Towards a Discrete Induced Spatial Curvature in Causal Sets

A Thesis

submitted to
Indian Institute of Science Education and Research Pune
in partial fulfillment of the requirements for the
BS-MS Dual Degree Programme

by

Abhishek Ravishankar

Indian Institute of Science Education and Research Pune
Dr. Homi Bhabha Road,
Pashan, Pune 411008, INDIA.

May, 2023

Supervisor: Sumati Surya

Certificate

This is to certify that this dissertation entitled **Towards a Discrete Induced Spatial Curvature in Causal Sets** towards the partial fulfilment of the BS-MS dual degree programme at the Indian Institute of Science Education and Research, Pune represents study/work carried out by Abhishek Ravishankar at Raman Research Institute, under the supervision of Sumati Surya, Professor, Department of Theoretical Physics, Raman Research Institute, during the academic year 2022-2023.

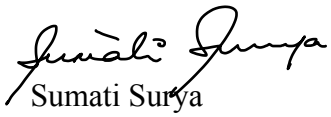

Sumati Surya

Committee:

Sumati Surya

Suneeta Vardarajan

This thesis is dedicated to everyone who believed in me, even when I didn’t believe in myself.

Declaration

I hereby declare that the matter embodied in the report entitled **Towards a Discrete Induced Spatial Curvature in Causal Sets** are the results of the work carried out by me at the Department of Theoretical Physics, Raman Research Institute, under the supervision of Sumati Surya, and the same has not been submitted elsewhere for any other degree.

Abhishek Ravishankar

Acknowledgments

I would like to thank my supervisor, Prof. Sumati Surya, for her constant support and valuable advice throughout my project. I am incredibly thankful to my parents, who have been a constant source of motivation, wholeheartedly supporting me in the pursuit of my interests. I would also like to acknowledge my friends, with whom my discussions have kept my curiosity alive.

I would like to acknowledge the Kishore Vaigyanik Protsahan Yojana (KVPY), which has supported my science education in college. I would also like to thank Raman Research Institute for hosting me over the course of my project and supporting me with their Visiting Student Program (VSP).

I would like to acknowledge Fleur Versteegen for the code that forms the framework for the numerical analysis in this work. The support and the resources provided by 'PARAM Brahma Facility' under the National Supercomputing Mission, Government of India at the Indian Institute of Science Education and Research (IISER) Pune are gratefully acknowledged.

Abstract

Causal set theory posits that, in order to derive a quantum theory of gravity, the causal structure of a spacetime is the fundamental object to be quantized. The discrete objects so obtained, known as causal sets, are equipped solely with a partial ordering, to enforce causality, and a measure, to define volumes of subsets. Spacetimes are conjectured to be causal sets under the limit of a discreteness scale at the Planck scale, and therefore, the manifold structure of a spacetime must be recoverable under this limit. In this vein, we attempt to characterise inextendible antichains, structures which form the causal set-analogues of Cauchy hypersurfaces. Taking inspiration from discrete space curvatures in the literature, we use an induced distance function defined on these structures to define a new measure of induced spatial curvature for inextendible antichains, which we have explicitly derived in the continuum limit for a 3-dimensional globally hyperbolic spacetime. We then use numerical techniques to implement this curvature, and to explore its feasibility, in the simplest system: that of flat inextendible antichains in causal sets approximated by Minkowski spacetime. This preliminary investigation into the characterisation of inextendible antichain curvature would not only add to the growing list of evidence supporting the fundamental conjecture of causal set theory, but would also provide a valuable tool to characterise causal sets, and would bring us one step closer to a causal set theoretic understanding of the initial value formulation of general relativity.

Contents

List of Tables

List of Figures

Part I

Background

Chapter 1

Causal Structure and Notation

We will begin by establishing the terminologies used throughout the rest of this work. We use natural units, wherein $c = 1$, as well as Einstein summation convention and abstract index notation as in [1]. Our treatment of causality roughly follows that in [2].

We consider d-dimensional Lorentzian manifolds (M, g_{ab}) with metrics of signature $(- + \cdots +)$. At any point $p \in M$, denote the **tangent space** to M at p by T_pM and, for $U \subset M$ the space of all smooth vector fields on U by $\Gamma(TU)$, where TU denotes the tangent bundle on U. Vectors $v^a \in T_pM$ are classified as follows:

$$\begin{aligned}
&\textbf{Timelike} \text{ if } g_{ab}v^a v^b < 0 \\
&\textbf{Null} \text{ if } g_{ab}v^a v^b = 0 \\
&\textbf{Spacelike} \text{ if } g_{ab}v^a v^b > 0
\end{aligned}$$

Timelike, null or **spacelike vector fields** are smooth vector fields $v^a : M \to TM$ such that $v^a(p)$ is timelike, null or spacelike respectively, $\forall p \in M$.

The timelike vectors in T_pM can be classified into two equivalence classes based on the following equivalence relation: for timelike vectors $v^a, w^a \in T_pM$, $v^a \sim w^a$ if $g_{ab}v^a w^b < 0$. We arbitrarily assign the labelling of **past-directed** and **future-directed** to the timelike vectors belonging to these classes. Timelike vector fields $v^a \in \Gamma(TM)$ are defined to be **past-directed** or **future-directed** if $v^a(p)$ is past-directed $\forall p \in M$ or if $v^a(p)$ is future-directed $\forall p \in M$ respectively. Null vectors can also be labeled as past-directed or future-directed as they are limits of the corresponding timelike vectors. Spacetime (M, g_{ab}) is said to be **time-orientable** if there exists a smooth specification of past and future across M, i.e., if there exists a future-directed timelike vector field

$t^a \in \Gamma(TM)$.

A **curve** is a continuous and smooth (or possibly piecewise-smooth) map of $\mathbb{R}$ (or a subset of it) into M, $\gamma : \mathbb{R} \to M$. The tangent vector field T^a to γ is used to define the notions of **timelike, null** and **spacelike curves**, as well as **past-directed** and **future-directed timelike curves**. A curve is **causal** if its tangent vector is always either timelike or null and is **future-directed null** or **past-directed null** if it is a causal curve with tangent vectors that are always future-directed or past-directed respectively.

A **trip** is a map of $\mathbb{R}$ (or a subset of it) into M, $\gamma : [a, b] \to M$ which is a piecewise future-directed timelike curve. A **trip from** x **to** y is a trip γ that starts at x and ends at y. Therefore γ consists of a set of points $x = x_0, x_1, \cdots, x_n = y$, where $n \geq 1$, and future-directed timelike segments $\gamma_{i-1\ i}$ from x_{i-1} to x_i for each $i = 1, \cdots, n$. A trip without a future (or past) endpoint is referred to as a **future-inextendible** (or **past-inextendible**) **trip** and one with neither endpoint is simply an **inextendible trip**. We say x **chronologically precedes** y iff there exists a trip from x to y, and denote this by $x \ll y$. A **causal trip** is defined similarly to a trip except for timelike curve segments being replaced by causal curve segments (that are possibly degenerate). We say x **causally precedes** y iff there exists a causal trip from x to y, and denote this by $x \preceq y$.[1] **Future-inextendible**, **past-inextendible** and **inextendible causal trips** can also be similarly defined. Note that due to the possibility of degenerate null curves, we could have $x = x_0, x_1 = x$. Therefore,

$$\boxed{x \preceq x \quad \forall x \in M \implies \text{Causal Precedence is a } \textbf{reflexive} \text{ relation}} \tag{1.1}$$

As all trips are causal trips, we also have

$$x \ll y \implies x \preceq y$$

Next, let $x \preceq y$ and $y \preceq z$ for $x, y, z \in M$. Then we have causal trips γ and σ consisting of sets of points $x = p_0, p_1, \cdots, p_m = y$ and $y = q_0, q_1, \cdots, q_n = z$ respectively, where $m, n \geq 1$, and future-directed causal curve segments $\gamma_{i-1\ i}$ and $\sigma_{i-1\ i}$ from p_{i-1} to p_i for each $i = 1, \cdots, m$ and q_{i-1} to q_i for each $i = 1, \cdots, n$ respectively. We can now construct the concatenated causal trip $\gamma * \sigma$ consisting of the set of points $x = r_0 = p_0, r_1 = p_1, \cdots, r_m = p_m = y = q_0, r_{m+1} = q_1, \cdots, r_{m+n} = q_n = z$ and future-directed causal curve segments $(\gamma * \sigma)_{i-1\ i} = \gamma_{i-1\ i}$ for $i = 1, \cdots, m$ and $(\gamma * \sigma)_{i-1\ i} =$

[1] The causal and chronological precedence relations can instead be defined with curves instead of trips, and this alternative definition is entirely equivalent, as is proven in [2], and more physical, although less convenient

$\sigma_{i-m-1\ i}$ for $i = m+1, \cdots, m+n$. Therefore,

$$\boxed{\begin{aligned}&\text{If } x \preceq y \text{ and } y \preceq z \implies x \preceq z \quad \forall x, y, z \in M \\ &\qquad\qquad \implies \text{Causal Precedence is a } \textbf{transitive} \text{ relation}\end{aligned}} \tag{1.2}$$

We define a **closed timelike (or causal) trip** to be a timelike (or non-degenerate causal) trip that is future-directed and closed. Spacetimes that contains no closed causal trips shall be referred to as **causal spacetimes**. In these spacetimes, if $x \preceq y$ and $y \preceq x$ for $x, y \in M$, then, by concatenating the associated future-directed causal paths, we obtain a closed causal trip if x, y are distinct events, leading to a contradiction. Therefore, in causal spacetimes,

$$\boxed{\begin{aligned}&\text{If } x \preceq y \text{ and } y \preceq x \implies x = y \quad \forall x, y \in M \\ &\qquad\qquad \implies \text{Causal Precedence is an } \textbf{antisymmetric} \text{ relation}\end{aligned}} \tag{1.3}$$

Relations that are reflexive, antisymmetric and transitive are called **non-strict partial orders** and a set with such a relation forms a **partially ordered set** or a **poset**. From eqs. (1.1) to (1.3), we see that causal, time-orientable spacetimes (M, g_{ab}) have a poset structure, referred to as the **Causal Structure Poset** $(M, \preceq)$ of (M, g_{ab}). This structure will play a key role in causal set theory, as will be seen in chapter 2.

For a point $p \in M$, the set $I^+ = \{x \in M | p \ll x\}$ is the **chronological future** of p, $I^- = \{x \in M | x \ll p\}$ is called the **chronological past** of p, $J^+ = \{x \in M | p \preceq x\}$ is called the **causal future** of p and $J^- = \{x \in M | \preceq p\}$ is called the **causal future** of p. For a set $S \subset M$, $I^+(S) = \bigcup_{x \in S} I^+(x)$ is the chronological future of S, $J^+(S) = \bigcup_{x \in S} J^+(x)$ is the causal future of S, and similarly for the pasts. [1] A spacetime M is said to be **future-distinguishing at** $p \in M$ if $I^+(p) \neq I^+(q)$ for each $q \in M$ with $q \neq p$; Spacetime M is said to be **future-distinguishing** if it is future-distinguishing at every point.

An **achronal set** $S \subset M$ is a subset of M wherein no two points of S are chronologically related, i.e., if $x, y \in S$, then $x \not\ll y$. For an achronal subset $S \subset M$, the **future** and **past domains of dependence** $D^{\pm}(S)$ as well as the **domain of dependence** $D(S)$ of S are defined as follows:

$$D^+(S) \equiv \{x \in M | \text{ every past-inextendible trip containing } x \text{ intersects } S\}$$
$$D^-(S) \equiv \{x \in M | \text{ every future-inextendible trip containing } x \text{ intersects } S\}$$

[1] We will, in general, no longer explicitly mention the past analogues of the quantities we describe.

$$D(S) \equiv \{x \in M | \text{ every inextendible trip containing } x \text{ intersects } S\} = D^{+}(S) \cup D^{-}(S)$$

An achronal subset $S \subset M$ such that $D(S) = M$ is defined to be a **Cauchy hypersurface**. A spacetime M which admits a Cauchy hypersurface is referred to as a **globally hyperbolic spacetime**. The Cauchy hypersurface will play an important role in this work.

Finally, let us touch upon a very useful map, known as the **exponential map**. For a point p in a Riemannian or Lorentzian manifold (M, g_{ab}), there is a very natural choice of chart for a neighbourhood U of p:
For tangent vector[2] $v \in T_pM$, consider the unique geodesic γ_v starting from p with tangent vector v at p. We may now consider the map **exponential map** $exp_p : T_pM \to M$ given by

$$exp_p(v) = \gamma_v(1)$$

While the presence of conjugate points may cause exp_p to not be injective, one can always find a small enough neighbourhood U of p within which exp_p is a diffeomorphism. This neighbourhood U of p is referred to as a Riemann normal neighbourhood of p and exp_p defines a natural coordinate system on U wherein the geodesics from p correspond to straight lines in T_pM, the metric tensor at p is given by η_{ab} and the Christoffel symbols vanish at p. This may be extended to a smooth map $exp : TM \to M$ from the tangent bundle of M to M. This map will be used in the discussion on Ollivier Curvature in chapter 3.

[2]Note that discussions involving the exponential map will not use abstract index notation and Einstein summation convention due to the confusing notation that it would result in

Chapter 2

Causal Set Theory: A Crash Course

2.1 Motivation

We now progress with the construction of causal set theory, in line with that in [3]. In order to motivate the approach of causal set theory, we begin by considering a time-orientable, causal, d-dimensional Lorentzian manifold (M, g_{ab}). As mentioned in chapter 1, these spacetimes admit a partially ordered structure, referred to as the causal poset $(M, \preceq)$. We may consider the structure-preserving maps of the causal structure poset, known as **causal bijections**. A causal bijection between $(M_1, \preceq_1)$ and $(M_2, \preceq_2)$ is a bijective map: $f : M_1 \to M_2$ such that

$$x \preceq_1 y \iff f(x) \preceq_2 f(y) \quad \forall\, x, y \in M_1$$

The importance of the causal structure poset is hinted at by the following theorem:

Hawking-King-McCarthy-Malament Theorem: *Consider d-dimensional spacetimes (M, g_{ab}) and $(\widetilde{M}, \tilde{g}_{ab})$ for $d > 2$, that are both future-distinguishing and past distinguishing. If there exists a causal bijection f between spacetimes M and $\widetilde{M}$, then the two spacetimes are conformally isometric, i.e., there exists a diffeomorphism $\varphi : M \to \widetilde{M}$ such that $\varphi^* (\tilde{g}_{ab}) = \Omega^2 \, g_{ab}$, where φ^* is the pullback induced by φ and Ω is a smooth function on M.*

This theorem highlights the importance of causal structure as, under reasonable restrictions on the spacetimes in consideration, the causal structure poset uniquely determines the spacetime structure up to a conformal factor. Therefore, in order to obtain a quantum theory of gravity, causal set theory chooses to quantise the causal structure of spacetime, into the fundamental object known as the **causal set**.

2.2 Fundamentals of CST

Definition (Causal Set). A **causal set** (or **causet**) $(C, \preceq)$ is a locally finite, partially ordered set, i.e., a set C with a relation $\preceq$ such that the following conditions are satisfied:

1. **Reflexivity**: $x \preceq x, \quad \forall\, x \in C$
2. **Antisymmetry**: $x \preceq y$ and $y \preceq x \implies x = y, \quad \forall\, x, y \in C$
3. **Transitivity**: $x \preceq y$ and $y \preceq z \implies x \preceq z, \quad \forall\, x, y, z \in C$
4. **Local Finiteness**: $\left|I\left[x, y\right]\right| < \infty, \quad \forall\, x, y \in C$, where $I\left[x, y\right] = Fut\left(x\right) \cap Past\left(y\right)$, where $|.|$ is the cardinality of a set and

$$\begin{aligned} Fut\left(x\right) &= \{z \in C | x \preceq z \text{ and } z \neq x\} \\ Past\left(x\right) &= \{z \in C | z \preceq x \text{ and } z \neq x\} \end{aligned} \tag{2.1}$$

The first three conditions ensure that the relation is a partial order, while local finiteness, the condition on the finiteness of **order intervals** $I\left[x, y\right]$, enforces discreteness. Since the HKMM Theorem can be summarised:

Causal Structure + Volume Element = Lorentzian Geometry,

that is, Lorentzian geometry is equivalent to a specification of causal structure and a volume element, this can be naturally generalised to the discrete case, known as the "CST Slogan":

Order + Number $\sim$ Lorentzian Geometry

We thus assume a fundamental correspondence between the number of elements in a region of a causal set and the continuum volume associated with that region. We are then led to the fundamental proposal [4]:

Quantum gravity is a quantum theory of causal sets, and a spacetime (M, g_{ab}) is an approximation of an underlying causal set C, i.e., $C \sim (M, g_{ab})$, where

(I) Order $\sim$ Causal Structure, and
(II) Number $\sim$ Volume Element.

Note that the set of all causal sets, which replaces the set of all spacetimes, will in general contain

causal sets that have no correspondence with any spacetime. Therefore, we need to make further precise the notion of a causal set being manifold-like, that is, the concept of the continuum approximation $C \sim (M, g_{ab})$. In order to do so, we define the following maps between causal sets and spacetimes:

Definition (Embedding). An **embedding** $\Phi : C \hookrightarrow M$ is an injective map such that

$$a \preceq b \iff \Phi(a) \preceq_M \Phi(b) \quad \forall\, a, b \in M$$

where $\preceq_M$ is the causal precedence relation in M and $\preceq$ is the partial ordering on C.

While embeddings preserve the poset structure in accordance with Correspondence (I), this is not sufficient to capture the continuum approximation. Therefore, in accordance with Correspondence (II), we define the following:

Definition (Faithful Embedding). A **faithful embedding** of causal set C into spacetime M is an embedding Φ such that $\Phi(C)$ is *uniformly distributed* in M at density ρ, where the *uniform distribution* is with respect to the spacetime volume measure. **Causal set C is said to approximate spacetime** (M, g_{ab}) if C faithfully embeds into (M, g_{ab}) at some density ρ.

If there exists such a faithful embedding of C into M, we denote this by $C \sim (M, g_{ab})$ and refer to C as a **manifold-like causal set**. We may associate with this embedding a **discreteness volume** $V_\rho = 1/\rho$ as well as a **discreteness scale** $\ell_\rho = \rho^{-1/d}$. Faithful embeddings provide a way of not only associating the order relation on the causal set with that on the spacetime, but they also allow us to associate with n-element subsets of C, the volume $n\,V_\rho$. In this way, we may adopt a statistical view of spacetimes: A spacetime is a macrostate corresponding to a certain family of causal sets which are its microstates. Although the images of the causal sets are required to be uniformly distributed in M, there are multiple prescriptions for embeddings that would allow for this, such as a regular lattice. However, since we require Correspondence (II) to be covariantly defined, embeddings such as a regular lattice would not serve our purpose.
The most natural choice of distribution then is a uniform random distribution for $\Phi(C)$, which results in Correspondence (II) being determined by a Poisson distribution, wherein the number of elements, **n**, of $\Phi(C)$ in a region $U \subset M$ of volume V is a Poisson random variable with probability distribution

$$P(n) = \frac{e^{-\rho V}\,(\rho V)^n}{n!} \tag{2.2}$$

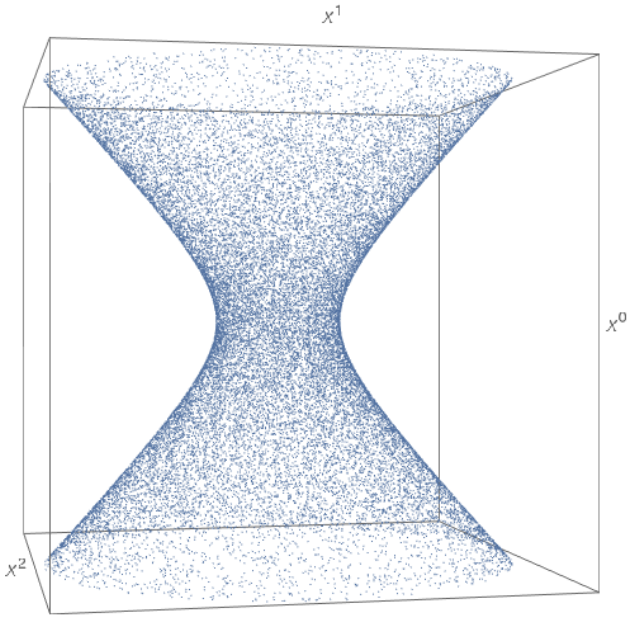

Figure 2.1: Poisson sprinkling of dS_2 embedded in 3-d Minkowski spacetime

In this way, the average number of elements in this region U is

$$\langle \mathbf{n} \rangle = \sum_{n=0}^{\infty} n\, P(n) = \rho V$$

allowing for the "Number $\sim$ Volume" correspondence of $n \sim \rho V$ to hold upon averaging. We may now describe how we generate causal sets from a spacetime, in a process known as the ***Poisson Sprinkling***:

In a Poisson sprinkling into a spacetime (M, g_{ab}) at density ρ, we sample points uniformly (with respect to the volume element) at random from M at density ρ to obtain a subset C. We then use the underlying poset structure of the manifold $(M, \preceq_M)$ to induce a partial ordering $\preceq$ onto C and generate a causal set $(C, \preceq)$.

Note that for a causal set obtained in this way, the natural embedding map $\Phi : C \hookrightarrow M$ is a faithful embedding. Therefore, from a spacetime (M, g_{ab}), using the Poisson sprinkling, we may obtain a family of causal sets $\mathcal{C}(M, \rho)$ which faithfully embed into M, forming the ensemble of microstates corresponding to macrostate of the spacetime, and averaging is to be done over this ensemble. We say that a **causal set C is approximated by spacetime** (M, g_{ab}) if C can be obtained from (M, g_{ab}) by a high probability Poisson sprinkling. For the sake of convenience, we shall refer to elements of $\mathcal{C}(M, \rho)$ as *sprinklings of M at (density ρ)*. The example of a sprinkling of 2-d deSitter spacetime embedded in an ambient 3-d Minkowski spacetime is shown in fig. 2.1.

2.3 Geometric Reconstruction

As causal set theory posits that a spacetime is an approximation of an underlying causal set, this causal set is supposed to contain all the physical structure of the spacetime. Therefore, in order have a self-consistent theory, it is required that if a causal set faithfully embeds at some sprinkling density into two spacetimes, that both the spacetime manifolds must have the same structure up to their discreteness scales. This consideration leads us to the Fundamental Conjecture of Causal Set Theory, the **Hauptvermutung**:

The Hauptvermutung of CST: *Causal set C can be faithfully embedded at density ρ_c into two spacetimes (M, g_{ab}) and $(\widetilde{M}, \tilde{g}_{ab})$ $\iff$ (M, g_{ab}) and $(\widetilde{M}, \tilde{g}_{ab})$ are approximately isometric*

By *approximately isometric*, we mean that they are isometric upto the discreteness scale ℓ_ρ, as all structure at smaller scales is unphysical; an artifact of the approximation of the causal set as a continuum. There have been a few attempts at a rigorous definition of such an approximate isometry[5, 6], although they remain but proposals.

The Hauptvermutung[1] implies that all manifold invariants $\mathcal{G}$ of a spacetime (M, g_{ab}) can be rewritten order theoretically, i.e., as order invariants $\mathcal{O}$, for the causal sets C that faithfully embed into the spacetime[2]. This motivates the program of **Geometric Reconstruction**, wherein order invariants $\mathcal{O}$ are constructed which correspond to manifold invariants $\mathcal{G}$. This correspondence would then ensure that if causal set C with order invariant $\mathcal{O}$ faithfully embeds into spacetime (M, g_{ab}) with manifold invariant $\mathcal{G}$, it can not embed into spacetime $(\widetilde{M}, \tilde{g}_{ab})$ with a different manifold invariant $\widetilde{\mathcal{G}}$. This results in a more limited version of the Hauptvermutung specific to order invariants:

$\mathcal{O}$-Hauptvermutung: *If causal set C with order invariant $\mathcal{O}$ faithfully embeds into spacetimes (M, g_{ab}) and $(\widetilde{M}, \tilde{g}_{ab})$, then $\mathcal{O}$ must correspond to the same manifold invariant $\mathcal{G}$ in both manifolds.*

Using the $\mathcal{O}$-Hauptvermutung, the larger the set of such geometric-order invariants that are constructed, the more credibility that is lent to the Fundamental Conjecture. Since this work lies well within the program of geometric reconstruction, we will specify in further detail the notions just presented.

[1] German for "main conjecture"

[2] Strictly speaking, these order invariants correspond to the ensemble $\mathcal{C}(M, \rho_c)$ as a whole, as the relation between the manifold structure and causal set structure is statistical in nature

A *labelling* of a causal set C is an injective map $\ell : C \to \mathbb{N}$, playing the role of a coordinate system for a causal set. To capture the notion of coordinate independence, we define an **order-invariant** of a finite causal set C as a function $\mathcal{O} : C \to \mathbb{R}$ invariant under change of labelling.[3]

In the context of manifold-like causal sets $C \in \mathcal{C}(M, \rho)$, there is a random variable $\mathcal{O}$ corresponding to every order invariant $\mathcal{O}$. The Hauptvermutung would suggest that the physically meaningful quantity $\langle \mathcal{O} \rangle$, obtained upon averaging over ensemble $\mathcal{C}(M, \rho)$, is equal to a manifold invariant $\mathcal{G}$ in the $\rho_c \to \infty$ limit. This limit, known as the **continuum limit**, although not entirely physical due to the local-finiteness of causal sets, is used as it represents the situation where the discreteness scale is small in comparison to the Planck scale. Although these order invariants are defined for all causal sets, as we will be attempting to reconstruct manifold curvatures, going ahead, we will restrict our attention to manifold-like causets. We now proceed to describe the primary object of our study, the inextendible antichain.

2.4 Cauchy Hypersurfaces and Inextendible Antichains

An important structure in the theory of general relativity is the Cauchy hypersurface. Upon specifying initial values and constraints on an 3-dimensional manifold Σ, they can be used to evolve the surface and generate a globally hyperbolic 4-dimensional solution to the vacuum Einstein equation within which Σ is a Cauchy hypersurface. Hence, the characterisation of Cauchy hypersurfaces, particularly their curvatures, is essential in order to translate this formulation into causal set theory.

We first require a causal set theoretic analogue of Cauchy hypersurfaces. From the definition as mentioned in chapter 1, we can derive the following properties of Cauchy hypersurfaces:

1. A Cauchy hypersurface Σ is a spacelike hypersurface
2. Every point not on the Cauchy hypersurface Σ lies either in the causal future $J^+(\Sigma)$ or causal past $J^+(\Sigma)$ of the surface.

These properties may be readily generalised into order-theoretic terms, resulting in the following definitions:

Definition (Antichain). An antichain is a subset $\mathcal{A} \subset C$ of causal set C consisting of unrelated elements, i.e.,

[3] Finiteness of C is imposed to ensure finiteness of the order invariant and in practice, can be enforced by restricting ourselves to compact neighbourhoods of the regions of interest

$$x \not\preceq y \quad \forall x, y \in \mathcal{A}$$

Definition (Inextendible Antichain). An inextendible antichain is an antichain $\mathcal{A} \subset C$ in causal set C such that

$$\forall x \in C \setminus \mathcal{A}, \exists y \in \mathcal{A} \quad \text{such that either } x \preceq y \text{ or } y \preceq x$$
$$\implies \forall x \in C \setminus \mathcal{A},\ x \in Fut(\mathcal{A}) \text{ or } x \in Past(\mathcal{A})$$

This allows for a decomposition of the form $C = Fut(\mathcal{A}) \sqcup \mathcal{A} \sqcup Past(\mathcal{A})$, allowing for the inextendible antichain to separate the causal set into disjoint future and past regions.
It is the inextendible antichain[4] that play the role of the Cauchy hypersurface in causal set theory. However, inextendible antichains are not complete analogues of Cauchy hypersurfaces as we will elaborate upon now. An important consequence of the definition of Cauchy hypersurfaces is that for Cauchy hypersurface Σ, every inextendible causal curve must intersect Σ. This property indicates the importance of a Cauchy hypersurface as a surface which provides a complete summary of its past and allows for a complete description of its future. However, the discreteness of causal sets and the extreme non-locality of causal links between elements imply that there is always the possibility of a causal link directly connecting an element $x \in Past(\mathcal{A})$ with an element $y \in Fut(\mathcal{A})$ without any intersection with $\mathcal{A}$. This is demonstrated in fig. 2.2, wherein a causal set sprinkled into 3-dimensional Minkowski spacetime contains an inextendible antichain embedding into Cauchy hypersurface $\Sigma \cong \mathbb{R}^2$. Nevertheless, this apparent failing of the inextendible antichain has not hindered efforts to reconstruct geometric properties of Cauchy hypersurfaces from inextendible antichains, and particularly, that of the **induced distance function on the Cauchy hypersurface**, as discussed in chapter 4.

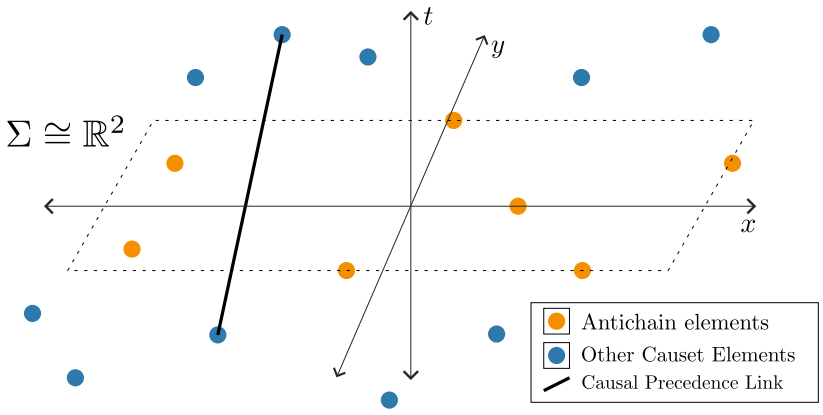

Figure 2.2: Failure of Inextendible Antichains as Complete analogues of Cauchy hypersurfaces

[4]In the rest of this work, whenever we refer to an object as an "antichain", we are still talking about an inextendible antichain, with "inextendible" truncated for brevity's sake

Chapter 3

Discrete Curvatures in the Literature

Curvature plays a key role in the theory of general relativity. The dynamical equations of motion in general relativity, the Einstein Equations, relate the intrinsic curvature of the spacetime manifold to the energy and matter within it. Specifically, we are motivated by the initial value formulation of general relativity, which involves the decomposition of a 4-dimensional spacetime in terms of a foliation of Cauchy hypersurfaces Σ_t and the specification of initial values on a particular Cauchy hypersurface Σ_0 to be evolved in time. The initial values specified are the dynamical variables, the induced metric tensor h_{ab} and extrinsic curvature K_{ab} of Σ_0, along with constraint equations between K_{ab} and the intrinsic scalar curvature ${}^{(3)}R$ of Σ_0. This indicates the importance of characterising the curvature of Cauchy hypersurfaces in globally hyperbolic spacetimes. However, these measures of curvature are heavily reliant on the powerful machinery provided by manifold structure and do not all generalise well to causal set theory. While there has been success in defining the scalar curvature R for causal sets [7], inextendible antichains have not been characterised in a similar way. We proceed to describe two measures of curvature in the literature that are better adopted to discrete structures.

3.1 Ollivier Curvature

Ollivier curvature is a measure of curvature introduced on metric spaces equipped with Markov chains (or probability measures, as we will use). In order to arrive at this quantity, we must begin by defining the quantity known as the **Wasserstein metric** (or the Kantorovich-Rubenstein distance of order one). We will eventually specialise to the case of Wasserstein metrics on Riemannian manifolds.

3.1.1 Wasserstein Metric

In order to motivate the definition of the Wasserstein metric, we begin by considering the problem of *optimal transport*:

We have a plot of land, modelled as a metric space (M, d), with a pile of sand, modelled as a measure μ on M, which is to be rearranged to another pile, modelled by measure ν on M. As the amount of sand is to be conserved, we normalise the measures to probability measures, i.e., $\int_M \mu(x)dV_x = \int_M \nu(y)dV_y = 1$. In order to specify the scheme used to rearrange the pile, we use a **transport plan** $\gamma : M \times M \to [0, \infty)$ such that $\gamma(x, y)$ is the amount of sand to move from x to y. Therefore, as we require the amount of sand moved from all of M to $y \in M$ to be the amount of sand at y in the final pile, we require[1]

$$\int_M \gamma(x, y)dV_x = \nu(y)$$

Similarly, as the amount of sand to be moved from $x \in M$ to every point in M is the amount of sand in the initial pile at x, we also require

$$\int_M \gamma(x, y)dV_y = \mu(x)$$

Therefore, we see that γ is a joint probability distribution whose marginal distributions are given by μ and ν. We denote the set of all such joint probability distributions of μ and ν by $\Gamma(\mu, \nu)$. Associated with transport, we have a cost function which determines the cost to move a unit amount of sand from one point to another. We will assume that this cost is determined by the distance the sand is to be transported, that is, that the cost to transport unit amount of sand from x to y is given by $d(x, y)$. The cost of a given transport plan γ, which we will refer to as the **transport distance** associated with γ, is then given by

$$\int_{M\times M} d(x, y)\gamma(x, y)\, dV_x\, dV_y$$

Therefore, in order to obtain the optimal transport distance, we have to minimise this cost over all allowed transport plans, leading to an optimal cost of

$$\inf_{\gamma\in\Gamma(\mu,\nu)} \int_{M\times M} d(x, y)\gamma(x, y)dV_x\, dV_y$$

[1] Integrals such as $\int dV_x$ and $\int dV_y$ are volume integrals

This optimal transport problem naturally leads us to the definition of the **Wasserstein metric**, a metric defined on the space of probability measures on a metric space.

Definition (Wasserstein Metric). Let (M, d) be a metric space. For probability measures μ and ν on M, the Wasserstein distance $W(\mu, \nu)$ is defined by

$$W(\mu,\nu) = \inf_{\gamma\in\Gamma(\mu,\nu)} \int_{M\times M} d(x,y)\gamma(x,y)\, dV_x\, dV_y \tag{3.1}$$

where $\Gamma(\mu, \nu)$ is the space of all joint probability measures on $M \times M$ with marginals μ and ν, that is,

$$\begin{aligned} \int_M \gamma(x,y)dV_y &= \mu(x) \\ \int_M \gamma(x,y)dV_x &= \nu(y) \end{aligned} \qquad \forall\, \gamma \in \Gamma(\mu,\nu) \tag{3.2}$$

The Wasserstein metric is actually a metric on the space of probability measures on a metric space, as proven in [8], and can be thought of as a distance between measures. While this metric has been utilised in many applications, we will focus on its use in the definition of Ollivier curvature in [9]

3.1.2 Curvature from the Wasserstein Metric

Definition (Ollivier Curvature). Consider a metric space (M, d). For $a, b \in M$, the **Ollivier curvature** $\kappa(a, b)$ is defined by:

$$\kappa(a,b) \equiv 1 - \frac{W(m_a^\epsilon, m_b^\epsilon)}{d(a,b)} \tag{3.3}$$

where m_a^ϵ and m_b^ϵ belong a family $\{m_x^\epsilon\}_{x\in M}$ of probability measures on M defined by:

$$m_x^\epsilon(y) \equiv \begin{cases} \frac{1}{vol(B_x^\epsilon)} & \text{if } y \in B_x^\epsilon \\ 0 & \text{else} \end{cases} \tag{3.4}$$

where

$$B_x^\epsilon \equiv \{z \in M \mid d(z,x) < \epsilon\} \tag{3.5}$$

We see that $\{m_x^\epsilon\}_{x\in M}$ is a family of uniform measures on balls of radius ϵ about every point in M, and the Ollivier curvature $\kappa(a, b)$ measures how much the distance between the uniform probability measures on balls centered at a and b deviates from the distance between a and b. We now proceed to explain the relationship between the Ollivier curvature and other, more familiar measures of curvature by specialising to the case of a Riemannian manifold.

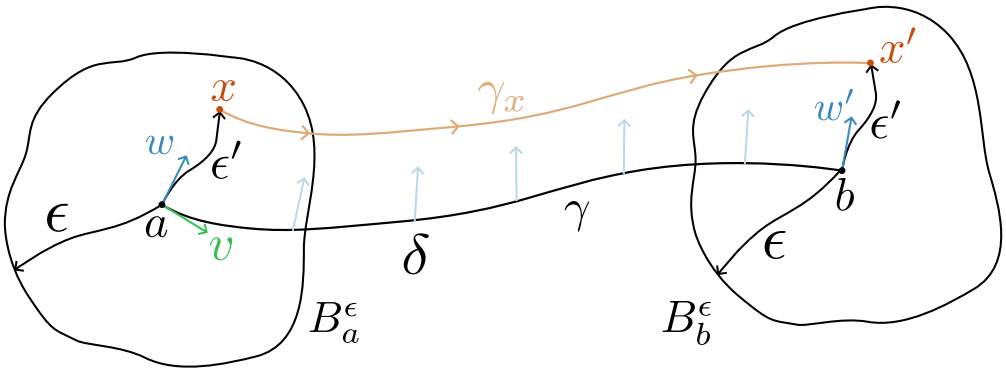

Figure 3.1: Optimal Transport Plan

For this discussion on the optimal transport plan, we will not use the abstract index notation and Einstein convention. Let us consider a D-dimensional Riemannian manifold (M, g) and the distance function d associated with the metric tensor g and points $a, b \in M$. We are concerned only with the case where the distance $d(a, b)$ between a and b is small enough. In this limit, for balls B_a^ϵ and B_b^ϵ in M with $\delta = d(a, b)$ small enough so that both balls lie within a convex normal neighbourhood, we may uniquely define the unit vector v along the geodesic γ from a to b, i.e., $b = exp_a(\delta v)$. Also, let $x \in B_a^\epsilon$ at distance $\epsilon' < \epsilon$ and $w \in T_aM$ such that $x = exp_a(\epsilon' w)$. We may use the covariant derivative on M to parallel transport w along γ from a to b, resulting in $w' \in T_bM$. Let us denote the point at distance ϵ' along w' from b as x', i.e., $x' = exp_b(\epsilon' w')$ and define a function $\Phi : B_a^\epsilon \to B_b^\epsilon$ given by

$$\Phi(x) = x'$$
$$\implies \Phi(x) = exp_{exp_a(\delta v)}(\epsilon' w')$$

where $x = exp_a(\epsilon' w)$ and w' is the unique parallel translate of w along γ at $b = exp_a(\delta v)$

This is illustrated in fig. 3.1, where γ_x is the unique geodesic from x to $x' = \Phi(x)$. It was shown in [9] that the optimal transport plan that is chosen in the Wasserstein distance $W(m_a^\epsilon, m_b^\epsilon)$ is the one that corresponds to the coupling of $x \in B_a^\epsilon$ solely with $\Phi(x) \in B_b^\epsilon$ as described above. The distance between x and x' is then given by

$$d(x, x') = \delta \left(1 - \frac{\epsilon'^2}{2} K(v, w) + \mathcal{O}(\epsilon'^3 + \epsilon'^2 \delta)\right) \tag{3.6}$$

where $K(v, w)$ is sectional curvature, given by

$$K(v, w) = \frac{R_{ijkl} v^i w^j v^k w^l}{v_i v^i \, w_j w^j - (v_i w^i)^2} \tag{3.7}$$

Using this transport plan, setting $\epsilon' = \epsilon$ and averaging eq. (3.6) over the set of all vectors $w \in T_a M$ that belong to a unit ball about the origin, results in the Wasserstein distance, given by:

$$W(m_a^\epsilon, m_b^\epsilon) = \delta \left(1 - \frac{\epsilon^2}{2\,(D+2)} R_{ij} v^i\, v^j + \mathcal{O}\left(\epsilon^3 + \epsilon^2 \delta\right)\right) \tag{3.8}$$

Therefore, we obtain an expression for the Ollivier curvature:

$$\kappa(a,b) = 1 - \frac{W(m_a^\epsilon, m_b^\epsilon)}{\delta} = \frac{\epsilon^2}{2\,(D+2)} R_{ij} v^i\, v^j + \mathcal{O}\left(\epsilon^3 + \epsilon^2 \delta\right) \tag{3.9}$$

This relation provides justification for $\kappa(a,b)$ being considered a measure of curvature. Note that from eq. (3.7), we have resumed use of abstract index notation and Einstein convention.
While this relation still hinges upon the manifold structure of M, the definition of Ollivier curvature, based on Wasserstein distance, is only dependent upon the distance function on M and therefore, can still be generalised to discrete spaces. We now discuss a relevant instance of this, in the system of random geometric graphs, as studied in [10].

3.1.3 Random Geometric Graphs

Random geometric graphs (RGGs) are graphs constructed from a Riemannian manifold (M, g_{ab}) as follows:

- Points are randomly sampled from M, uniformly with respect to the volume element on M, through a Poisson point process at number density n. This generates the vertex set V of the graph.

- Each vertex $v \in V$ is then connected to every other vertext $v' \in V$ for which $d(v, v') < t$, where t is a constant threshold for the graph known as the **connection radius** of the graph, and d is the distance function on M generated by the metric tensor g_{ab}. Each such edge is then given the weight $d(v, v')$. This results in the edge set E of the graph and completes the description of a weighted graph G.

In the resulting RGG G, the idea was to calculate Ollivier curvature under the continuum limit $n \to \infty$ and the limits of vanishing ball radius and inter-center radius. In order to do so, a fixed point x^* and a tangent vector $v^a \in T_x M$ are chosen. The second center y_n^* is chosen along the geodesic from x^* along vector v^a, at distances $d(x^*, y_n^*) = \delta_n$ such that

$$\lim_{n\to\infty} \delta_n = 0 \tag{3.10}$$

A random geometric graph is then sampled from M and the points x^*, y_n^* are added to the graph vertices V and appropriate vertices are added based on the connection radius ϵ_n, which is also defined to be a function of number density such that it vanishes under the continuum limit. This results in a random graph $G_n = \mathbb{G}_n(x^*, y_n^*, \epsilon_n)$, referred to as a **rooted random graph** on M, parameterised by number density n. Note that the functional forms of δ_n, ϵ_n are yet to be specified. In order to define balls on the graph, a graph distance function d_{G_n} is defined wherein, for $x, y \in G_n$, $d_{G_n}(x, y)$ is the length of the shortest path in the weighted graph G_n, leading to a metric space (G_n, d_{G_n}). The balls of radius r centered at x^*, y_n^* are then defined to be the sets of G_n's vertices lying within graph distance r from x^*, y_n^* respectively, that is, $B^r_{x^*} = \left\{ z \in G_n \,|\, d_{G_n}(z, x^*) < r \right\}$ and $B^r_{y_n^*} = \left\{ z \in G_n \,|\, d_{G_n}(z, y_n^*) < r \right\}$ respectively. For the purpose of defining the Ollivier curvature, we consider balls $B^{\delta_n}_{x^*}$ and $B^{\delta_n}_{y_n^*}$, that is, the ball radii are set equal to the inter-center distance, so that both the ball radii and the inter-center distance vanish under the continuum limit, uniting all three limits mentioned previously.

Having defined balls $B^{\delta_n}_{x^*}$ and $B^{\delta_n}_{y_n^*}$ on G_n, we now define the uniform measures $m^{\delta_n}_{x^*}, m^{\delta_n}_{y_n^*}$ by:

$$\begin{aligned} m^{\delta_n}_{x^*}(z) &\equiv \begin{cases} \frac{1}{|B^{\delta_n}_{x^*}|} & \text{if } z \in B^{\delta_n}_{x^*} \\ 0 & \text{else} \end{cases} \\ m^{\delta_n}_{y_n^*}(z) &\equiv \begin{cases} \frac{1}{|B^{\delta_n}_{y_n^*}|} & \text{if } z \in B^{\delta_n}_{y_n^*} \\ 0 & \text{else} \end{cases} \end{aligned} \tag{3.11}$$

Finally, the graph Ollivier curvature is defined as in eq. (3.3):

$$\kappa_G(x^*, y_n^*) \equiv 1 - \frac{W_G(m^{\delta_n}_{x^*}, m^{\delta_n}_{y_n^*})}{\delta_n} \tag{3.12}$$

where W_G is the Wasserstein metric on the metric space (G_n, d_{G_n}). For this setup, the following theorem holds, as was proven in [11]:

Theorem: *For $D \geq 2$, let (M, g_{ab}) be a D-dimensional smooth, orientable, connected and compact Riemannian manifold, $x^* \in M$ and $v^a \in T_{x^*}M$. For $\epsilon_n = \Theta\left(\log(n)^a n^{-\alpha}\right)$ and $\delta_n = \Theta\left(\log(n)^b n^{-\beta}\right)$ as $n \to \infty$, where*

$$0 < \beta \leq \alpha, \quad \alpha + 2\beta \leq \frac{1}{D}$$

and $a \leq b$ *if* $\alpha = \beta$ *and* $\min\{a, a+2b\} > \frac{2}{D}$ *if* $\alpha + 2\beta = \frac{1}{D}$.

Let $y_n^* \in M$ *be the point at distance* δ_n *along the direction* v^a *and* $G_n = \mathbb{G}_n(x^*, y_n^*, \epsilon_n)$ *be a rooted random graph on* M*. Then given the graph distance function* d_{G_n} *and the family of uniform probability measures* $\left\{m_z^{\delta_n}\right\}_{z\in G_n}$*, the graph Ollivier curvature satisfies the following:*

$$\lim_{n\to\infty} \mathbb{E}\left[\left|\frac{2(D+2)\,\kappa(x^*, y_n^*)}{\delta_n^2} - R_{ij}v^i v^j\right|\right] = 0 \tag{3.13}$$

where $\mathbb{E}[.]$ *is the expectation value on the sample space of rooted random graphs* G_n*.*

This result relates quantities of two distinct systems: the manifold M and the random geometric graphs G_n. Moreover, this system of random geometric graphs on manifold (M, g_{ab}) bears a striking resemblance to that of inextendible antichains in causal sets that are approximated by Cauchy hypersurface (Σ, h_{ab}) in (M, g_{ab}); Although the weights of the edges of RGGs are directly inherited from the manifold while those of the inextendible antichain edges are determined by the predistance function, both the graphs have cutoff-dependent connectivity, determined by the connection radius and mesoscale cutoff respectively. Therefore, while RGGs do not feel the effects of discrete asymptotic silence, eq. (3.13) does hint at the possibility of the continuum convergence of a similarly defined inextendible antichain Ollivier curvature to a manifold curvature.

However, as we will elaborate upon further in chapter 6, the optimisation involved in determining the Wasserstein distance on inextendible antichains is a problem in linear programming, which can prove computationally expensive to calculate for causal sets of sufficient size. Therefore, we now describe a related quantity that we will evaluate numerically.

3.2 Quantum Ricci Curvature

We now follow the discussion of an alternate measure of discrete curvature in [12], which deals with curvatures on simplicial manifolds, in the Causal Dynamical Triangulation approach to quantum gravity. In chapter 3, if eq. (3.6) were averaged over the unit sphere in the tangent space instead of the unit ball, with $\epsilon' = \epsilon$, we get the expression:

$$\delta\left(1 - \frac{\epsilon^2}{2D}R_{ij}v^i\,v^j + \mathcal{O}\left(\epsilon^3 + \epsilon^2\delta\right)\right)$$

where D is the dimension of the Riemannian manifold. Therefore, even this quantity, although not an Ollivier curvature, exhibits a limiting behaviour similar to that of the Ollivier curvature, scaled

by a different constant. However, this quantity suffers the disadvantage of not translating well to simplicial manifolds due to the very limited convexity radius in such structures. Therefore, they proposed a more robust measure of distance between S_a^ϵ and S_b^ϵ, the spheres of radius ϵ about points $a, b \in M$: the average distance $\bar{d}$

$$\bar{d}(S_a^\epsilon, S_b^\epsilon) = \frac{1}{vol(S_a^\epsilon)} \frac{1}{vol\,(S_b^\epsilon)} \int_{x \in S_a^\epsilon} \sqrt{h\,(x)}\, d^{D-1}x \int_{x' \in S_b^\epsilon} d(x, x')\, \sqrt{h\,(x')}\, d^{D-1}x' \tag{3.14}$$

where

$$S_a^\epsilon \equiv \{x \in M | d(x, a) = \epsilon\}\,, \tag{3.15}$$

S_b^ϵ being defined similarly, h and h' are the determinants, in the coordinate systems $\{x^\mu\}$ and $\{x'^\mu\}$, of the induced metric tensor h_{ab} on the spheres S_a^ϵ and S_b^ϵ respectively and vol is the codimension-1 volume. While this does not define a true distance function as $\bar{d}(S_a^\epsilon, S_a^\epsilon) \neq 0$, the ratio $\bar{d}/\delta$, as shown in [13] for $D = 2, 3, 4$ conveys information about curvature:

$$\frac{\bar{d}}{\delta} = \begin{cases} 1.5746 + \delta^2 \left(-0.1440\, R_{ij} v^i\, v^j + \mathcal{O}(\delta)\right), & \text{for } D = 2 \\ 1.6250 + \delta^2 \left(-0.0612\, R_{ij} v^i\, v^j - 0.0122\, R + \mathcal{O}(\delta)\right), & \text{for } D = 3 \\ 1.6524 + \delta^2 \left(-0.0469\, R_{ij} v^i\, v^j - 0.0067\, R + \mathcal{O}(\delta)\right), & \text{for } D = 4 \end{cases}$$

Therefore, analogous to the Ollivier curvature, the **quantum Ricci curvature** $K_q(a, b)$ is defined as

$$\frac{\bar{d}(S_a^\delta, S_b^\delta)}{\delta} = c_q \left(1 - K_q(a, b)\right) \tag{3.16}$$

where, as before, the sphere radii are set equal to the inter-center distance, and c_q is a constant dependent on the metric space. This quantity naturally generalises to discrete spaces as the average distance can be defined in them as:

$$\bar{d}(S_a^\epsilon, S_b^\epsilon) = \frac{1}{|S_a^\epsilon|} \frac{1}{|S_b^\epsilon|} \sum_{x \in S_a^\epsilon} \sum_{x' \in S_b^\epsilon} d(x, x') \tag{3.17}$$

Part II

The Structure of Inextendible Antichains

Chapter 4

The Volume-Induced Distance Function

We now describe the construction of the distance function on inextendible antichains, as defined in [14]. Since the antichain itself contains no structure (due to the lack of any causal relation within it), the antichain is thickened into the future and structure is imposed onto it from the causal relations within this thickening. We will first define a "**Predistance Function**" that is induced on the Cauchy hypersurface $\Sigma \subset M$ from the causal poset $(M, \preceq)$, and then proceed to define a distance function using the predistance. We then translate these definitions into the language of order theory in order to extend the definition to causal sets, and then mention some key features of the distance function obtained on inextendible antichains.

4.1 Inducing a Distance Function onto Cauchy Hypersurface

We begin by providing the general construction we will use to define the predistance, before motivating it with relevant cases. We will work with a time-orientable globally hyperbolic causal spacetime (M, g_{ab}) with volume element vol and Cauchy hypersurface (Σ, h_{ab}), where h_{ab} is the metric induced on Σ. For $a, b \in \Sigma$, consider their causal futures $J^+(a)$ and $J^+(b)$, and their common causal future

$$J\left(a,b\right) \equiv J^+(a) \cap J^+(b) \tag{4.1}$$

For $p \in J\left(a,b\right)$, we call the region

$$J\left(\Sigma,p\right) \equiv J^+\left(\Sigma\right) \cap J^-(p)$$

the *"shadow of p"*. we define the **Suspended Volume function** $V : J(a,b) \to [0,\infty)$ by

$$V(p) \equiv vol\left(J\left(\Sigma,p\right)\right) = vol\left(J^+\left(\Sigma\right) \cap J^-(p)\right) \tag{4.2}$$

We then minimise $V(p)$ over $J(a,b)$ to define

$$V(a,b) \equiv \inf_{p \in J(a,b)} V(p) \tag{4.3}$$

Finally, we define the **predistance** $\tilde{d} : \Sigma \times \Sigma \to [0,\infty)$ by

$$\boxed{\tilde{d}(a,b) \equiv 2\left(\frac{V(a,b)}{\zeta_D}\right)^{1/D}} \tag{4.4}$$

where

$$\boxed{\zeta_D \equiv \frac{\pi^{\frac{D-1}{2}}}{D\,\Gamma\left(\frac{D+1}{2}\right)}} \tag{4.5}$$

To motivate the construction, we will begin by considering the simplest case: an extrinsically flat Cauchy hypersurface in the D-dimensional Minkowski spacetime $\mathbb{M}^D$. We will then move on to constant curvature Cauchy hypersurfaces in $\mathbb{M}^D$ before defining the complete distance function for Cauchy hypersurfaces in general spacetimes.

4.1.1 Inertial Cauchy Hypersurface in Minkowski Spacetime

In D-dimensional Minkowski spacetime $\mathbb{M}^D$, let $(\Sigma, h_{ab}) \cong (\mathbb{R}^{d-1}, \delta_{ab})$ be an inertial Cauchy hypersurface, i.e., a Cauchy hypersurface with extrinsic curvature $K_{ab} \equiv \nabla_a \xi_b = 0$, where ξ_b is the unit future-directed timelike vector field normal to Σ and ∇ is the covariant derivative in $\mathbb{M}^D$. Given points $a, b \in \Sigma$, the suspended volume function is illustrated by fig. 4.1.

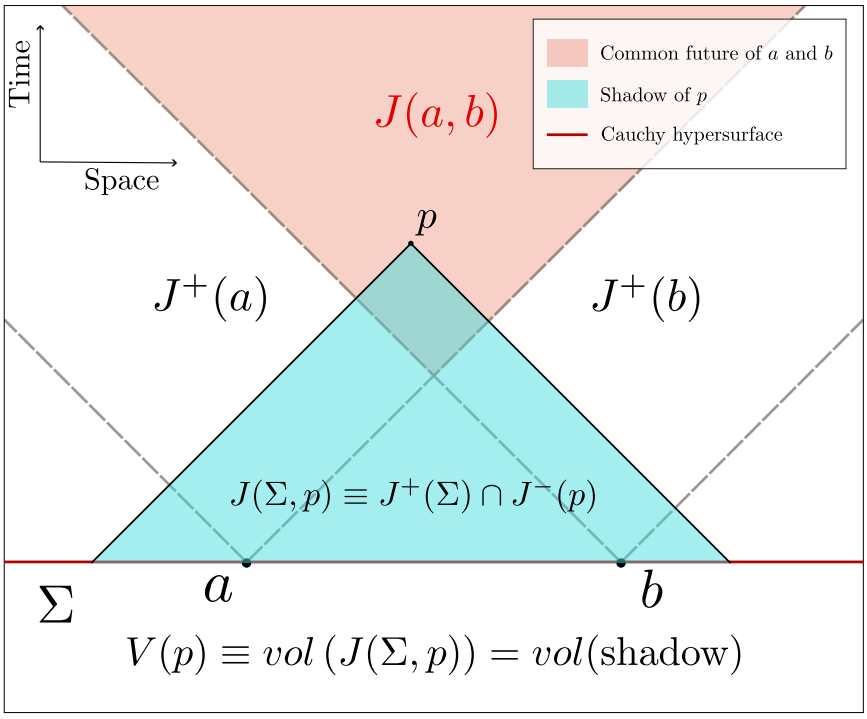

Figure 4.1: Suspended Volume Function Construction in Minkowski Spacetime

If we set the coordinate system such that $a = (0, -T, 0, \cdots, 0)$ and $b = (0, T, 0, \cdots, 0)$, we see that at

$$\mathbf{r}_m = (T, 0, 0, \cdots, 0) \in \mathcal{H}(a, b) = \partial J^+(a) \cap \partial J^+(b)$$

the suspended volume function takes on its minimum value as the points a and b become antipodal points on the $D-2$-sphere that forms the set $\partial B_\Sigma(\mathbf{r}_m) \subset \Sigma$, where $B_\Sigma(\mathbf{r}_m) = (J^-(p) \cap \Sigma)$ is the base of the cone of suspended volume. The volume then corresponds to that of a D-dimensional right cone of base radius T and proper time T from Σ to $\mathbf{r}_m$. This takes the value:

$$\begin{aligned} V(a, b) &= V(\mathbf{r}_m) = \zeta_D T^D \\ \text{where} \quad \zeta_D &= \frac{\pi^{\frac{D-1}{2}}}{D\,\Gamma\left(\frac{D+1}{2}\right)} \end{aligned} \tag{4.6}$$

where the value of constant ζ_D is derived in appendix A. Therefore, we see that

$$\tilde{d}(a, b) = 2\left(\frac{V(\mathbf{r}_m)}{\zeta_D}\right)^{1/D} = 2T = d_h(a, b)$$

where $d_h(a, b)$ is the distance under the induced metric on Σ. This is illustrated in fig. 4.2.

Although in this case, the predistance function is equal to the distance function, this happens because of the lack of extrinsic curvature in Σ and intrinsic curvature in M. Therefore, in order to motivate the general construction of the distance function, next we look at the case of Cauchy hypersurfaces with constant extrinsic curvature in Minkowski spacetime.

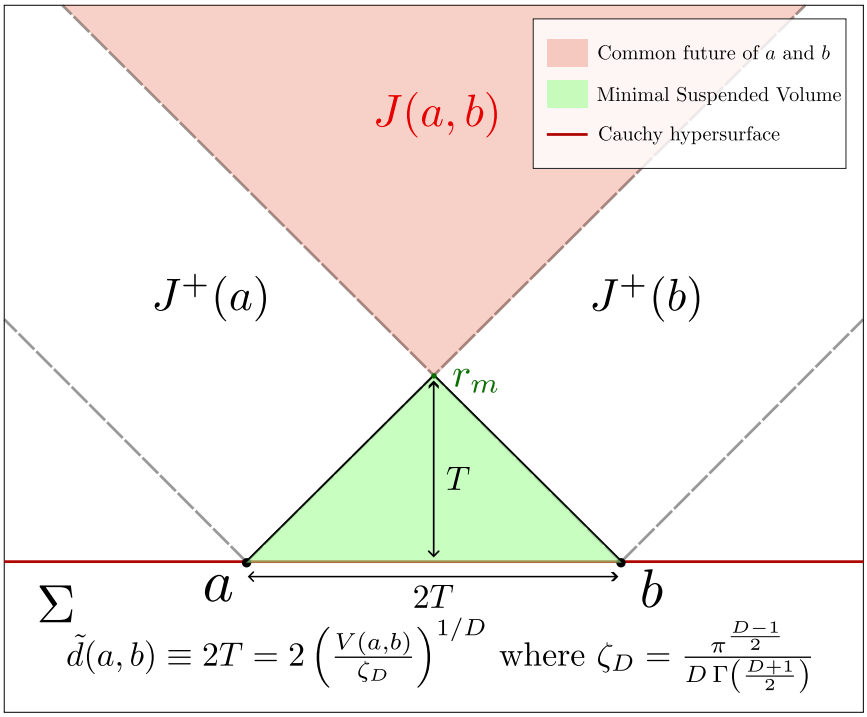

Figure 4.2: Minimal Suspended Volume in Minkowski Spacetime

4.1.2 Constant Extrinsic Curvature Cauchy Hypersurface in Minkowski Spacetime

A Cauchy hypersurface (Σ, h_{ab}) with constant extrinsic curvature K_{ab} corresponds to a co-dimension 1 hyperboloid. We will denote the trace of extrinsic curvature by $K \equiv h^{ab}K_{ab}$. We continue to define the predistance function $\tilde{d}$ by eqs. (4.2) to (4.5) and, similar to the previous case, as we are in Minkowski spacetime, there exists an element $\mathbf{r}_m \in J(a,b)$ which realises the minimal value in eq. (4.3). However, now the predistance function will not equal the induced distance on the hypersurface as the suspended volume no longer takes the shape of a perfect cone. Rather, it now takes the form of an inverted "icecream cone" which is scooped out for $K > 0$ and topped off for $K < 0$. Therefore, the predistance function will instead take the value

$$\tilde{d}(a,b) = 2T'$$

where T' is not equal to the proper time T from p to the hypersurface Σ. In order to understand the quantity T', we construct an inertial hypersurface Σ' such that $vol(J(\Sigma', r_m)) = vol(J(\Sigma, r_m))$. Then the suspended volume $J(\Sigma', r)$ has a height T' and a flat base $B_{\Sigma'}(\mathbf{r}_m)$ of diameter $2T'$. This is illustrated in fig. 4.3. This results in a predistance function of the form

$$\tilde{d}(a,b) = 2T' = 2T\left(1 + \text{sgn}\,(K)\,\epsilon(a,b)\right)$$

where sgn is the sign function and $\epsilon(a,b)$ is a function of a, b and K. It can be seen that if we restrict a and b to be within a small enough neighbourhood $N \subset \Sigma$, ϵ can be bounded. Also, it can be shown, as in [14], for a and b with induced distance $d_h(a,b)$ sufficiently small, the predistance is given by:

$$\tilde{d}(a,b) = d_h(a,b)(1 + \text{sgn}(K)\epsilon'(a,b))$$

for a small function ϵ'. Therefore, as long as a and b are **restricted to a small enough neighbourhood $N \subset \Sigma$, $\tilde{d}$ approximates d_h to arbitrary precision**.

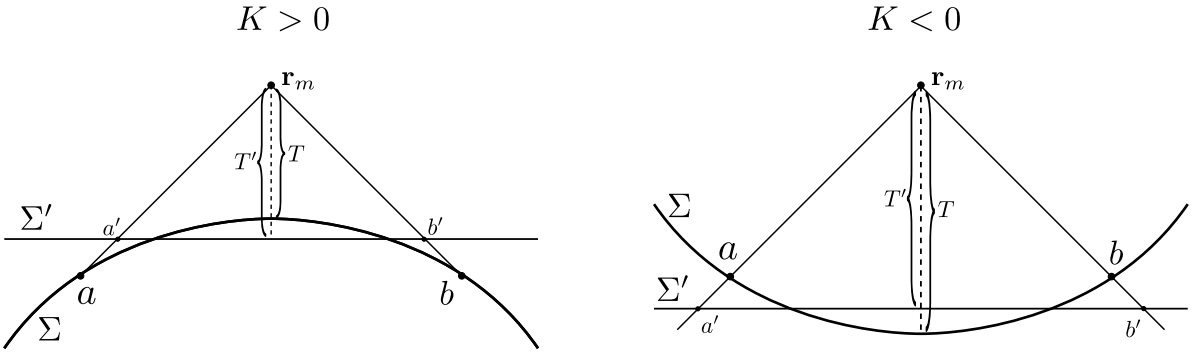

Figure 4.3: Curved hypersurface in Minkowski spacetime

4.1.3 Compact Cauchy Hypersurface in a General Spacetime

We now proceed to the most general case we will consider: a compact Cauchy hypersurface (Σ, h_{ab}) in globally hyperbolic D-dimensional spacetime (M, g_{ab}). As learnt from the previous case, we consider the situation where a and b are sufficiently close to each other and showcase the behaviour of the predistance function upto leading order. This analysis was performed in [14], using a combination of Riemann Normal Neighbourhoods (RNN) M_a of a in Σ, RNN N_a of a in M, constructed to contain the domain of dependence $D(M_a)$ and Gaussian Normal Neighbourhood (GNN) N_Σ of Σ in M, referred to as a Gaussian-Riemann Neighbourhood (GRN) wherein b is chosen within the GRN. The predistance function $\tilde{d}$ sill remains defined by eqs. (4.2), (4.4) and (4.5), while eq. (4.3) is slightly modified so that

$$V(a,b) = \inf_{p \in \mathcal{H}(a,b)} V(p)$$

where $\mathcal{H}(a,b) = \partial J^+(a) \cap \partial J^+(b) \cap D(M_a)$. Due to this construction, $\mathcal{H}(a,b)$ is compact, allowing the suspended volume function to take its minimum value at some point $\mathbf{r}_m \in \mathcal{H}(a,b)$.

Moreover, as calculated in [15], the construction allows for a series expansion of the suspended volume function eq. (4.2) as:

$$\begin{aligned} V(r) &= V_\eta(r)\left(1 + \frac{D}{2\,(D+1)} K\,(r_0)\,T\right) + \mathcal{O}\left(T^{D+2}\right) \\ \implies \tilde{d}(a,b) &= 2T\left(1 + \frac{1}{2\,(D+1)} K\left(\mathbf{r}_{m0}\right) T\right) + \mathcal{O}\left(T^3\right) \end{aligned}$$

where r_0 is the unique point on Σ from which originates a perpendicular geodesic to $r \in \mathcal{H}(a,b)$ as allowed for by GNN N_Σ, $\mathbf{r}_{m0} \in \Sigma$ is this point corresponding to $\mathbf{r}_m$, T is the proper time from r_0 to r along this geodesic and $V_\eta(r)$ is the flat suspended volume function from section 4.1.1, given by eq. (4.6). We will refer to the trace of extrinsic curvature as K as, upto leading order, K is constant within M_a. The induced distance $d_h(a,b)$ can also be expanded on the basis of dimensional analysis to obtain an error function $\epsilon\,(a,b)$

$$\begin{aligned} & d_h(a,b) = 2T\,(1 + \alpha K T) + \mathcal{O}(T^3) \\ \implies & \epsilon\,(a,b) \equiv \tilde{d}(a,b) - d_h(a,b) = 2\left(\frac{1}{2\,(D+1)} - \alpha\right) K T^2 + \mathcal{O}\left(T^3\right) \end{aligned} \tag{4.7}$$

where α is a dimension-dependent parameter. As before, from eq. (4.7), it is clear that as long as we restrict a and b so that the GRN is small enough, the error can be bounded to arbitrary precision. It is to be noted that compactness was not necessary for the discussion so far, but will become important in the following discussion on the definition of the distance function.

4.1.4 Distance from Predistance

So far, we have defined a predistance function for compact Cauchy hypersurfaces (Σ, h_{ab}) in globally hyperbolic D-dimensional spacetimes, which can be used to approximate the induced distance d_h within small enough neighbourhoods. We would now like to use this predistance function to construct a distance function on Σ. To do so, we first define the following:

Definition (k-path from a to b)**.** A k-path $\gamma^{(W_k)}$ from a to b is a discretised path consisting of an ordered set of points $W_k \equiv (a = w_0, w_1, \cdots, w_k = b)$ where $w_i \in \Sigma$, $\forall i \in \{0, 1, \cdots, k\}$. The length of the k-path is defined in terms of the predistance function as

$$d_{W_k}(a, b) \equiv \sum_{i=0}^{k-1} \tilde{d}(w_i, w_{i+1}) \tag{4.8}$$

We denote the set of all k-paths from a to b for all finite k by $\Gamma(a, b)$. We would like to use k-path lengths to construct a distance function. In order to define a true distance function, triangle inequality must be obeyed. In order to do so, we may attempt to define the distance function to be

$$d(a, b) \stackrel{?}{=} \inf_{\gamma^{(W_k)} \in \Gamma(a,b)} d_{W_k}(a, b)$$

However, as this definition does not take into account the extrinsic curvature of Σ, it will almost always result in a 1-path directly from a to b, not conforming sufficiently to the surface Σ. In order to ensure that the paths under consideration conform to the surface, we restrict the set of paths from $\Gamma(a, b)$ to

$$\Gamma_\ell(a, b) = \left\{ \gamma^{(W_k)} \middle| \tilde{d}(w_i, w_{i+1}) < \ell,\ \forall i \in \{0, 1, \cdots, k-1\},\ \forall k \in \mathbb{N} \right\}$$

where we have now bounded path-segment lengths to be less than ℓ, referred to as a **mesoscale cutoff**.

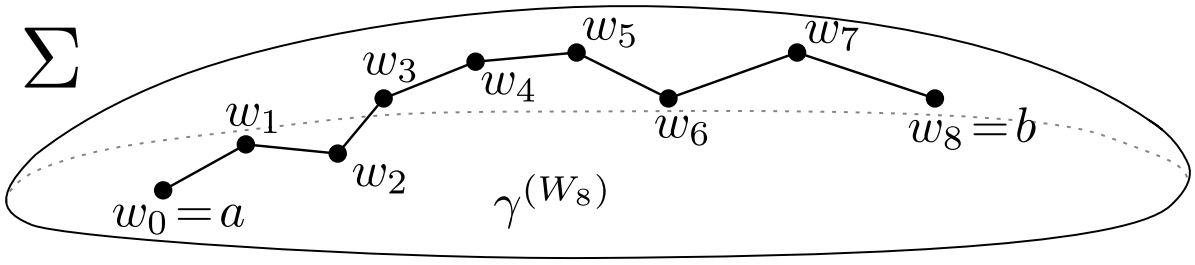

Figure 4.4: An 8-path from a to b

Therefore, we may now define a family of distance functions:

Definition (Distance function). The **distance function** with mesoscale cutoff ℓ is the function $d : \Sigma \times \Sigma \to [0, \infty)$ given by

$$d_\ell(a, b) \equiv \inf_{\gamma^{(W_k)} \in \Gamma_\ell(a,b)} d_{W_k}(a, b) \tag{4.9}$$

From the triangle inequality, we can say that the infimum in eq. (4.9) attempts to minimise k the number of segments, while the mesoscale cutoff prevents k from being too low by restricting each segment to a small enough neighbourhood. The compactness of Σ implies that we may cover Σ with a finite number of GRNs, $\{N_\alpha\}_\alpha$. Taking ϵ_α to be the supremum of predistance error $\epsilon(p, q)$ defined by 4.7 over all $p, q \in N_\alpha$, the finiteness of the cover of Σ implies that

$$\epsilon_\Sigma = \sup_\alpha \epsilon_\alpha$$

is finite. As every path consists of a finite number of segments, the distance function error is bounded, as long as the mesoscale cutoff ℓ is chosen so that $\tilde{d}(p, q) < \ell$, $\forall p, q \in N_\alpha$. From eq. (4.7), as the intrinsic curvature does not contribute to error at leading order, a useful length scale to inform a choice of mesoscale cutoff ℓ is the **extrinsic curvature radius**, given by $\ell_K = 1/K$. We focus more on length scales in 4.3.2.

While the discussions on the predistance and distance functions make extensive use of the manifold properties of the Cauchy hypersurface and the spacetime, the definitions of the functions only involve causal structure and spacetime volumes, allowing a natural generalisation to manifold-like causal sets.

4.2 The Inextendible Antichain Distance Function

We now proceed to consider a manifold-like causal set C approximated by a D-dimensional spacetime (M, g_{ab}) at embedding density ρ, with a compact Cauchy hypersurface Σ whose causal set analogue is an inextendible antichain $\mathcal{A}$. Motivated by the definition of the predistance function given in eqs. (4.2) to (4.5), the antichain predistance function $\tilde{d} : \mathcal{A} \times \mathcal{A} \to [0, \infty)$ is defined as follows:

Given $a, b \in \mathcal{A}$, we define their common future

$$F(a, b) \equiv Fut(a) \cap Fut(b) \tag{4.10}$$

where $Fut(a)$ and $Fut(b)$ are defined as in eq. (2.1).

The suspended volume function $V : F(a,b) \to [0,\infty)$ is then defined

$$\begin{gathered} N(c) \equiv |Fut(\mathcal{A}) \cap Past(c)| \quad \text{where} \quad Fut(\mathcal{A}) \equiv \bigcup_{x \in \mathcal{A}} Fut(x) \\ V(c) \equiv N(c)/\rho \end{gathered} \tag{4.11}$$

Just as in 4.3, we proceed by defining

$$V(a,b) \equiv \inf_{c \in F(a,b)} V(c) \tag{4.12}$$

The predistance function $\tilde{d}$ is defined as in eqs. (4.4) and (4.5)

$$\tilde{d}(a,b) \equiv 2\left(\frac{V(a,b)}{\zeta_D}\right)^{1/D} \tag{4.13}$$

where

$$\zeta_D \equiv \frac{\pi^{\frac{D-1}{2}}}{D\,\Gamma\left(\frac{D+1}{2}\right)}$$

Since Σ is compact, $\mathcal{A}$ is a finite set. Also due to local finiteness, $F(a,b)$ is at most countably infinite. Therefore, for every number $V' > 0$, there are a finite number of elements $c \in F(a,b)$ such that $V(c) \leq V'$. We may then find the smallest V' such that there is only one $\mathbf{e} \in F(a,b)$ with $V(\mathbf{e}) = V'$. This element $\mathbf{e}$ is then the element that realises the minimisation in eq. (4.12), playing the role of $\mathbf{r}_m$ in the causal set case. Therefore, the predistance can be redefined as

$$\boxed{\tilde{d}(a,b) \equiv 2\left(\frac{V(\mathbf{e})}{\zeta_D}\right)^{1/D}} \tag{4.14}$$

Having defined the predistance, to define the distance function, we proceed identically to section 4.1.4, defining k-paths γ^{W_k} from a to b in terms of ordered sets of elements
$W_k \equiv (a = w_0, w_1, \cdots, w_k = b)$ where $w_i \in \mathcal{A}$, $\forall i \in \{0,1,\cdots,k\}$. With a **mesoscale cutoff** ℓ, the set of all admissible paths is defined

$$\Gamma_\ell\,(a,b) = \left\{\gamma^{(W_k)} \middle| \tilde{d}(w_i, w_{i+1}) < \ell,\ \forall i \in \{0,1,\cdots,k-1\},\ \forall k \in \mathbb{N}\right\}$$

and the **family of distance functions** $d_\ell : \mathcal{A} \times \mathcal{A} \to [0,\infty)$ is given by

$$\boxed{d_\ell(a,b) \equiv \inf_{\gamma^{(W_k)} \in \Gamma_\ell(a,b)} d_{W_k}(a,b)} \tag{4.15}$$

4.3 Properties of the Inextendible Antichain Functions:

In the case of the predistance and distance functions on inextendible antichains, there are a few further subtleties to be addressed. Beyond the continuum-based errors in the causal set predistance function, arising from the deviation of the underlying geometry from that of an inertial hypersurface in flat spacetime, there is also a source of error unique to the causal set case: **stochastic fluctuations**. As the suspended volume function is a Poisson random variable, there is an inherent randomness associated with its value. This error associated with randomness is overcome by the ensemble averaging that is performed in order to obtain physical quantities. However, there is another effect of stochasticity that is not overcome by averaging: **Discrete Asymptotic Silence**.

4.3.1 Discrete Asymptotic Silence

In a causal set C with inextendible antichain $\mathcal{A}$, that approximates, at density ρ, spacetime (M, g_{ab}) with Cauchy hypersurface Σ, let us consider points $a, b \in \mathcal{A}$, which are close enough with respect to an appropriate mesoscale cutoff. Let us refer to the common future and suspended volume function in the continuum as F_M and V_M respectively, and the common future and suspended volume function in the causal set as F_C and V_C respectively. It is to be noted that $F_C \subset F_M$ as the partial ordering in C is induced from the causal structure of M. The causal set minimising element $\mathbf{e}$ will almost always result in a larger continuum suspended volume than the continuum minimising element $\mathbf{r}_m$ as, if

Proposition 1 *The causal set volume minimising element* $\mathbf{e}$ *will almost always result in a larger continuum suspended volume than the continuum volume minimising element* $\mathbf{r}_m$*, i.e.,*

$$V_M(\mathbf{r}_m) \leq V_M(\mathbf{e})$$

*where the equality only holds in a measure-*0 *subset of the sample space of sprinklings* $\mathcal{C}(M, \rho)$

Proof. The continuum minimising element $\mathbf{r}_m$ is unique, and therefore this singleton set will only be realised as $\mathbf{e}$ in a measure-0 subset of the sample space. Therefore, we may proceed under the assumption that $\mathbf{r}_m$ and $\mathbf{e}$ are distinct in general.
Let us assume that

$$V_M(\mathbf{r}_m) > V_M(\mathbf{e})$$

Then,

$$F_C \subset F_M \text{ and } \mathbf{e} \in F_C \quad \Longrightarrow \quad \mathbf{e} \in F_M$$

contradicting the premise that $\mathbf{r}_m$ minimises V_M in F_M. □

Furthermore, due to the Poisson Sprinkling, for a fixed **e**, we know $V_C(\mathbf{e})$ is a Poisson random variable such that $\langle V_C(\mathbf{e})\rangle = V_M(\mathbf{e})$. Therefore, we come to the conclusion that, for a given $a, b \in \mathcal{A}$,

$$\boxed{V_M(\mathbf{r}_m) < \langle V_C(\mathbf{e})\rangle}$$

Therefore, due to the stochastic nature of the sprinklings, the causal set predistance function always over-approximates the continuum predistance. Note that the discreteness of the causal set and its embedding in the spacetime at density ρ results in an intrinsic length scale, referred to as the **discreteness scale**, given by $\ell_\rho \equiv 1/\rho$. This scale defines the minimum length scale of structures in the manifold that can be considered physical. If a and b are separated by length scales much larger than ℓ_ρ, the large sizes of the sets involved in the predistance calculation dampen the relative effects of the stochastic fluctuations that separate **e** from $\mathbf{r}_m$. This results in a relatively small error in predistance.

However, if a and b are separated by length scales comparable to ℓ_ρ, the effects of the stochastic fluctuations become more significant. This leads to large separation between **e** and $\mathbf{r}_m$, resulting in a significant fractional error in the causal set predistance $\tilde{d}$ with respect to the continuum distance d_h. This phenomenon of large deviation of the predistance from the continuum distance is referred to as **Discrete Asymptotic Silence**[16]. This is illustrated in fig. 4.5, where $V_M(\mathbf{e})$ and $V_M(\mathbf{r}_m)$ are shaded to give one an idea of the aforementioned overestimation of suspended volume.

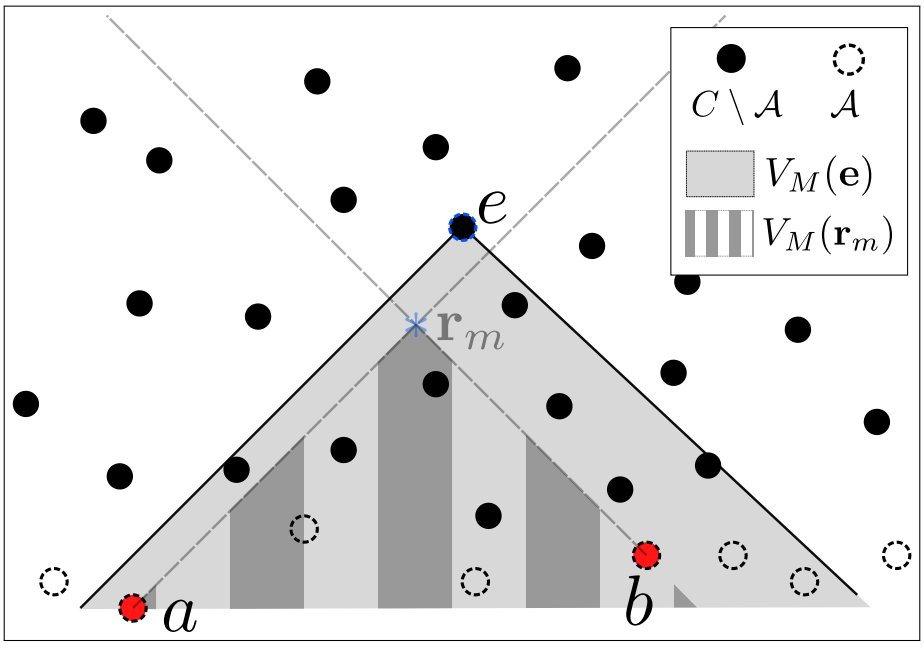

Figure 4.5: Discrete Asymptotic Silence

Discrete Asymptotic Silence, or DAS will play a significant role in the rest of this work, leading to errors that persist on averaging. Although the effects of DAS are observed at all length scales, it plays a very significant role within a length scale which we refer to as the **Discrete Asymptotic Silence Scale** ℓ_{DAS}. We now proceed to discuss all the length-scales involved in our analysis so far.

4.3.2 Separation of Length-Scales

So far, there are four length-scales of relevance to our analysis of the distance function on inextendible antichains:

- Discreteness scale ℓ_ρ
- Discrete Asymptotic Silence scale ℓ_{DAS}
- Mesoscale cutoff ℓ
- Extrinsic Curvature scale ℓ_K

The discreteness scale is the smallest meaningful length scale, and the discrete asymptotic silence scale characterises the inner extent of the region within which the predistance function accurately approximates the continuum distance. As the mesoscale cutoff defines the outer extent of the region within which the predistance can be used as an accurate distance function, it must be chosen so that

$$\ell_\rho < \ell_{DAS} \ll \ell$$

Moreover, as the extrinsic curvature radius determines the region beyond which the effects of extrinsic curvature become significant, it sets an upper bound on the mesoscale cutoff:

$$\ell_\rho < \ell_{DAS} \ll \ell \ll \ell_K$$

Note: If we work in the regime within ℓ, it is sufficient to use the predistance function instead of the distance function. As a modified version of Dijkstra's algorithm is required in order to perform the optimisation in eq. (4.15) in practice, this regime allows for a computationally inexpensive method to use the distance function. We will take advantage of this in numerical simulations, as discussed in chapter 6.

Having introduced the distance function, we shall revisit the topic of curvature, specialising to inextendible antichains. Taking inspiration from the curvatures described in chapter 3, we propose a curvature to characterise inextendible antichains with.

Chapter 5

A New Volume-Induced Ricci Curvature

In chapter 3, we have mentioned two curvatures suitable for use on discrete systems:

1. **Ollivier curvature**, defined on metric spaces and studied extensively on random geometric graphs

2. **Quantum Ricci curvature**, defined on metric spaces and introduced for use on simplicial manifolds

Ollivier curvature provides the most promising way to characterise inextendible antichain curvature, due to its extensive analysis in RGGs which have strong connections to inextendible antichains equipped with the distance function. Let us elaborate further upon the calculation of Wasserstein distances in inextendible antichains: We have a Lorentzian manifold (M, g_{ab}) with a Cauchy hypersurface (Σ, h_{ab}). As we require an ensemble of sprinklings into (M, g_{ab}) with fixed points a^* and b^* to center balls at, we choose the set of sprinklings $\mathcal{C}(M, \rho)$ that embed into (M, g_{ab}), with inextendible antichain $\mathcal{A}$, and then add a^* and b^* to each sprinkling and inextendible antichain. This results in a set of **rooted sprinklings** $\mathcal{C}(M, \rho, a^*, b^*)$ with **rooted inextendible antichains** $\mathcal{A}$. We will go on to use these objects without explicitly referring to them as *rooted*. The inextendible antichain $\mathcal{A}$ is equipped with the distance function d_ℓ with an appropriate mesoscale cutoff ℓ. We then define a ball of radius ϵ centered at $a \in \mathcal{A}$ as

$$B_a^\epsilon \equiv \{x \in \mathcal{A} \,|\, d_\ell(x, a) < \epsilon\} \tag{5.1}$$

Given a ball B_a^ϵ, the uniform measure on it is defined as

$$m_a^\epsilon(z) = \begin{cases} \frac{1}{|B_a^\epsilon|} & \text{if } z \in B_a^\epsilon \\ 0 & \text{else} \end{cases} \tag{5.2}$$

which is well-defined due to the local-finiteness of causal sets. We now have a family of measures $\{m_a^\epsilon\}_{a\in\mathcal{A}}$ and, given a causal set $C \in \mathcal{C}(M, \rho, a^*, b^*)$, we may define the Wasserstein metric:

$$W_{\mathcal{A}}(m_{a^*}^\epsilon, m_{b^*}^\epsilon) = \inf_{\gamma\in\Gamma(m_{a^*}^\epsilon, m_{b^*}^\epsilon)} \sum_{x\in\mathcal{A}}\sum_{x'\in\mathcal{A}} d_\ell(x, x')\,\gamma(x, x') \tag{5.3}$$

where $\gamma : \mathcal{A}\times\mathcal{A} \to [0, \infty)$ is a joint probability distribution such that:

$$\begin{aligned} \sum_{x'\in\mathcal{A}} \gamma(x, x') &= m_{a^*}^\epsilon(x) \\ \sum_{x\in\mathcal{A}} \gamma(x, x') &= m_{b^*}^\epsilon(x') \end{aligned} \tag{5.4}$$

and $\Gamma(m_{a^*}^\epsilon, m_{b^*}^\epsilon)$ is the space of all such joint distributions. The Ollivier curvature is again given by

$$\kappa(a^*, b^*) = 1 - \frac{W_{\mathcal{A}}(m_{a^*}^\epsilon, m_{b^*}^\epsilon)}{\delta} \tag{5.5}$$

where $\delta = d_\ell(a^*, b^*)$. In practice, we will have a finite causal set C with a finite antichain $\mathcal{A}$ of size N. In this case, γ can be thought of as a vector valued function, particularly, $\gamma \in \mathbb{R}^{N^2}$. However, there are constraints on the function's value due to the non-negativity of γ and eqs. (5.4). The first consideration restricts γ to have only non-negative components but does not decrease the dimensionality of the allowed solution space. However, as each equation in eqs. (5.4) corresponds to N linear equality constraints, this leads to a reduction in dimensionality by $2N$. This results in $\Gamma(m_{a^*}^\epsilon, m_{b^*}^\epsilon)$, the allowed solution space, being a convex, $(N^2 - 2N)$-dimensional subset of $\mathbb{R}^{N^2}$, and the optimal solution γ of the objective function

$$\sum_{x\in\mathcal{A}}\sum_{x'\in\mathcal{A}} d_\ell(x, x')\,\gamma(x, x')$$

existing at some point on the boundary. This is a problem in the field of linear programming, which can be solved numerically using interior-point methods or simplex methods. However, in practice, this requires the calculation of the complete distance function (or, at the very least, the complete predistance function) on $\mathcal{A}$. Moreover, the most efficient linear programming algorithms[17] are

of roughly quadratic time complexity in the number of variables $n = N^2$. Therefore, while the Ollivier curvature is a promising quantity to characterise inextendible antichains with, due to these computational challenges that we will face in studying the continuum limit, we will not calculate it numerically in this work. Instead, we will proceed in the vein of 3.2; We will use an average distance, **specialising to the D = 3 case** and conjecturing behaviour in the general case.

5.1 A New Dimensionless Ricci Curvature: The Continuum Case

Due to its computational simplicity, we would like to use an average distance to measure curvature, beginning with the continuum. Therefore, we consider a D-dimensional spacetime (M, g_{ab}) with a Cauchy hypersurface (Σ, h_{ab}) and the distance function d on Σ associated with the induced Riemannian metric tensor h_{ab}. For $p, p' \in \Sigma$ where $d(p, p') = \delta$ is small enough, as in section 3.1.2, we could work with spheres S^ϵ_p and $S^\epsilon_{p'}$ in Σ as defined in eq. (3.15). However, as spheres in an antichain are measure-0 sets, in general, they will not be sampled in any sprinkling. Therefore, instead of the prescription of [12], we use balls B^ϵ_p and $B^\epsilon_{p'}$ of radius ϵ as defined in eq. (3.5), that is,

$$\begin{aligned} B^\epsilon_p &\equiv \{z \in \Sigma \,|\, d(z,p) < \epsilon\} \\ B^\epsilon_{p'} &\equiv \{z \in \Sigma \,|\, d(z,p') < \epsilon\} \end{aligned} \tag{5.6}$$

Instead of the Wasserstein distance, we use the average distance $\bar{d}\,(p, p'; \epsilon)$ between the balls B^ϵ_p and $B^\epsilon_{p'}$ in Σ:

$$\boxed{\bar{d}\,(p,p';\epsilon) \equiv \frac{1}{vol\left(B^\epsilon_p\right)} \frac{1}{vol\left(B^\epsilon_{p'}\right)} \int\limits_{x \in B^\epsilon_p} \sqrt{h(x)}\, d^{D-1}x \int\limits_{x' \in B^\epsilon_{p'}} \sqrt{h(x')}\, d^{D-1}x'\; d(x,x')} \tag{5.7}$$

where $\sqrt{h}$ is the volume element of Σ. Note that this corresponds to the transportation distance associated with the transport plan given by the product measure $\gamma_P : \Sigma \times \Sigma \to [0, \infty)$

$$\gamma_P\,(x, x') \equiv m^\epsilon_p(x)\, m^\epsilon_{p'}(x') \tag{5.8}$$

where m^ϵ_p and $m^\epsilon_{p'}(x')$ are the uniform probability measures on the balls B^ϵ_p and $B^\epsilon_{p'}$, as in eq. (3.4). As this work will primarily deal with the case of 3-dimensional spacetimes, we now consider the case of $D = 3$. In this case, the ratio of this average distance with δ, $\frac{\bar{d}(p,p';\epsilon)}{\delta}$, can then be expanded

in the small parameter[1] $R\delta^2$, where R is the Ricci scalar at p:

$$\frac{\bar{d}\left(p,p';\epsilon\right)}{\delta} = c_P + \tilde{c}_R\, R\delta^2 + \mathcal{O}\left(R^2\delta^4\right) \tag{5.9}$$

where c_P is the value of this ratio in the Euclidean case. Therefore, analogous to eq. (3.16), we may use the leading non-trivial term in this expansion to define a **continuum dimensionless Ricci curvature (cDRC)** $K_P\left(p,p'\right)$:

$$\boxed{K_P\left(p,p'\right) \equiv 1 - \frac{1}{c_P}\frac{\bar{d}\left(p,p';\epsilon\right)}{\delta}} \tag{5.10}$$

where the constant c_P is a dimension-dependent constant that is, in general, also dependent on the ratio μ of the ball radii to the inter-center distance:

$$\mu \equiv \frac{\epsilon}{\delta} \tag{5.11}$$

Note that while μ was set to 1 in the definition of quantum Ricci curvature in section 3.2, we allow it to be a free parameter. We now explicitly perform this calculation for the $D = 3$ case, as described below.

5.1.1 Dimensionless Ricci Curvature Calculation for $D = 3$

We will calculate the average distance as in eq. (5.7), and hence the manifold volume-induced Ricci curvature as in eq. (5.10), for the case of a 3-dimensional spacetime (M, g_{ab}) with 2-dimensional Cauchy hypersurface (Σ, h_{ab}) and distance function d on Σ associated with the metric h_{ab}, where h_{ab} is the induced metric on Σ. This calculation will follow the similar calculation performed in [18] for the quantum Ricci curvature. Before proceeding with the calculation, we will mention here a few useful properties, as in [19], of Riemann normal coordinates (RNCs) in a Riemann normal neighbourhood $U \subset \Sigma$, with a typical length scale L, centred about point $p \in \Sigma$:

- For a point $x \in U$ with RNCs x^μ, the metric tensor $h_{\mu\nu}\left(x\right)$ at x can be expressed as

$$h_{\mu\nu}\left(x\right) = \delta_{\mu\nu} - \frac{1}{3}R_{\mu\alpha\nu\beta}x^\alpha x^\beta + \mathcal{O}\left(L^3\right) \tag{5.12}$$

  where $R_{\mu\alpha\nu\beta} = R_{\mu\alpha\nu\beta}\left(p\right)$, the curvature tensor at p.

- For points $p_1, p_2 \in U$ with RNCs x_1^μ and x_2^μ respectively, the squared distance between p_1 and p_2 is given by

[1] For $D > 3$, R will not completely characterise the hypersurface's intrinsic curvature, and the expansion may vary

$$d^2(p_1,p_2) = \delta_{\mu\nu}\left(\Delta x_{12}^{\mu}\right)\left(\Delta x_{12}^{\nu}\right) - \frac{1}{3}R_{\mu\alpha\nu\beta}x_1^{\mu}x_2^{\alpha}x_1^{\nu}x_2^{\beta} + \mathcal{O}\left(L^5\right) \tag{5.13}$$

where $\Delta x_{12}^{\mu} = x_1^{\mu} - x_2^{\mu}$. Furthermore, the Riemann normal neighbourhood is defined such that

$$\boxed{R\,L^2 \ll 1} \tag{5.14}$$

- As U is centred about p, it is the origin of the RNC system and hence $h_{\mu\nu}(p) = \delta_{\mu\nu}$ and $d^2(p,p_1) = \delta_{\mu\nu}x_1^{\mu}x_1^{\nu}$

We consider point $p \in \Sigma$ and an RNN, U in Σ, centred about p, with a characteristic length L. Point p' is chosen in U with distance $\delta = d(p,p')$ separating p and p' and the vector $v \in T_p\Sigma$ from p to p'. We then consider ϵ-radius balls centred at p and p':

$$\begin{aligned} B_p^{\epsilon} &= \{z \in \Sigma \,|\, d(z,p) < \epsilon\} \\ B_{p'}^{\epsilon} &= \{z \in \Sigma \,|\, d(z,p') < \epsilon\} \end{aligned} \tag{5.15}$$

where ϵ is a small enough radius to allow for B_p^{ϵ} and $B_{p'}^{\epsilon}$ to be fully contained in the previously mentioned RNN. This construction is illustrated in fig. 5.1. In this RNN, we further define two polar coordinate systems: (r,θ) centred about p, and (r',θ') centred about p', and as r and r' are defined as the geodesic distances to p and p' respectively, we will use these to coordinatise balls B_p^{ϵ} and $B_{p'}^{\epsilon}$ respectively. As this RNN is centred at p, the ball B_p^{ϵ} centred at p has a coordinate description identical to that in a flat space that is, $q \in B_p^{\epsilon}$ in the Cartesian RNC is given by:

$$q = (r\cos\theta, r\sin\theta)\,, \qquad \text{where } r \in [0,\epsilon)\,,\ \theta \in [0,2\pi]$$

Centre p' of ball $B_{p'}^{\epsilon}$ is chosen along the x-axis of the Cartesian RNC system, that is,

$$p' = (\delta, 0)$$

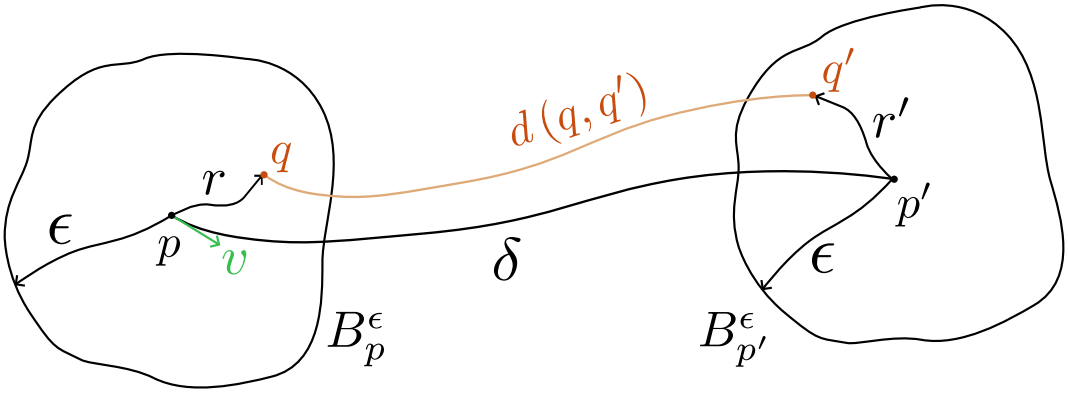

Figure 5.1: Average Distance Construction

As the ball $B^{\epsilon}_{p'}$ is not centred about p, for $q' \in B^{\epsilon}_{p'}$, its Cartesian coordinate description will be modified as follows:

$$q' = (\delta + w(r', \theta') \cos\theta', w(r', \theta') \sin\theta'), \quad \text{where } r' \in [0, \epsilon),\ \theta' \in [0, 2\pi]$$

where $w(r', \theta')$ is a function that encodes the deformation of the ball due to curvature. For $q' \in B^{\epsilon}_{p'}$, as the distance between p' and q' is r', we have

$$r'^2 = d^2(p', q') = w^2(r', \theta') \left[1 - \frac{\delta^2}{3} R_{1212} \sin^2\theta' + \mathcal{O}(L^3)\right]$$
$$\implies w(r', \theta') = r' \left[1 - \frac{\delta^2}{3} R_{1212} \sin^2\theta' + \mathcal{O}(L^3)\right]^{-\frac{1}{2}}$$

To derive an expression to the order we desire, we need only expand $w(r', \theta')$ upto order δ^2, resulting in

$$w(r', \theta') = r' \left[1 + \frac{\delta^2}{6} R_{1212} \sin^2\theta'\right] + \mathcal{O}(L^4) \tag{5.16}$$

Moreover, as the Riemann curvature of a 2-dimensional manifold has only one independent component, the value of the curvature tensor at p is given in terms of the Ricci scalar R at p by:

$$R = 2\, R_{1212} \tag{5.17}$$
$$\implies \boxed{w(r', \theta') = r' \left[1 + \frac{R\delta^2}{12} \sin^2\theta'\right] + \mathcal{O}(L^4)} \tag{5.18}$$

We now proceed to find the distance between points $q \in B^{\epsilon}_{p}$ and $q' \in B^{\epsilon}_{p'}$:

$$\boxed{d^2 \equiv d^2(q, q') = \delta_{\mu\nu} \left(\Delta x^{\mu}_{q\,q'}\right) \left(\Delta x^{\nu}_{q\,q'}\right) - \frac{1}{3} R_{\mu\alpha\nu\beta} x^{\mu}_{q} x^{\alpha}_{q'} x^{\nu}_{q} x^{\beta}_{q'} + \mathcal{O}(L^5)} \tag{5.19}$$

where
$$x^1_q = r\cos\theta, \qquad x^2_q = r\sin\theta,$$
$$x^1_{q'} = \delta + w(r', \theta')\cos\theta', \qquad x^2_{q'} = w(r', \theta')\sin\theta'$$

We begin with evaluating the first term in eq. (5.19):

$$\delta_{\mu\nu} \left(\Delta x^{\mu}_{q\,q'}\right) \left(\Delta x^{\nu}_{q\,q'}\right) = \left(x^1_q - x^1_{q'}\right)^2 + \left(x^2_q - x^2_{q'}\right)^2$$
$$= (\delta + w(r', \theta')\cos\theta' - r\cos\theta)^2 + (w(r', \theta')\sin\theta' - r\sin\theta)^2$$
$$\left(x^1_q - x^1_{q'}\right)^2 = (\delta + w(r', \theta')\cos\theta' - r\cos\theta)^2 \tag{5.20}$$

$$= \delta^2 \left[1 + \left(\frac{r'}{\delta}\right)\cos\theta' - \left(\frac{r}{\delta}\right)\cos\theta + \frac{R\delta^2}{12}\left(\frac{r'}{\delta}\right)\sin^2\theta'\cos\theta' + \mathcal{O}\left(L^3\right)\right]^2 \tag{5.21}$$

$$= \delta^2 \left(1 + \left(\frac{r'}{\delta}\right)\cos\theta' - \left(\frac{r}{\delta}\right)\cos\theta\right)^2 \left[1 + \frac{\left(\frac{r'}{\delta}\right)\sin^2\theta'\cos\theta'}{1 + \left(\frac{r'}{\delta}\right)\cos\theta' - \left(\frac{r}{\delta}\right)\cos\theta}\frac{R\delta^2}{12} + \mathcal{O}\left(L^3\right)\right]^2 \tag{5.22}$$

$$\begin{aligned} &= \delta^2 \Bigg[\left(1 + \left(\frac{r'}{\delta}\right)\cos\theta' - \left(\frac{r}{\delta}\right)\cos\theta\right)^2 \\ &\quad + \frac{R\delta^2}{6}\left(\frac{r'}{\delta}\right)\sin^2\theta'\cos\theta'\left(1 + \left(\frac{r'}{\delta}\right)\cos\theta' - \left(\frac{r}{\delta}\right)\cos\theta\right) + \mathcal{O}(L^3)\Bigg] \end{aligned} \tag{5.23}$$

Similarly,

$$\left(x_q^2 - x_{q'}^2\right)^2 = \left(w\left(r', \theta'\right)\sin\theta' - r\sin\theta\right)^2 \tag{5.24}$$

$$\begin{aligned} &= \delta^2 \Bigg[\left(\left(\frac{r'}{\delta}\right)\sin\theta' - \left(\frac{r}{\delta}\right)\sin\theta\right)^2 \\ &\quad + \frac{R\delta^2}{6}\left(\frac{r'}{\delta}\right)\sin^3\theta'\left(\left(\frac{r'}{\delta}\right)\sin\theta' - \left(\frac{r}{\delta}\right)\sin\theta\right) + \mathcal{O}\left(L^3\right)\Bigg] \end{aligned} \tag{5.25}$$

Therefore, the first term of eq. (5.19) is given by:

$$\delta_{\mu\nu}\left(\Delta x^{\mu}_{q\,q'}\right)\left(\Delta x^{\nu}_{q\,q'}\right) = d^2_{\text{Eu}} + d^2_{R'} \tag{5.26}$$

where,

$$\boxed{d^2_{\text{Eu}} = \delta^2\left[\left(1 + \frac{r'}{\delta}\cos\theta' - \frac{r}{\delta}\cos\theta\right)^2 + \left(\frac{r'}{\delta}\sin\theta' - \frac{r}{\delta}\sin\theta\right)^2\right]} \tag{5.27}$$

$$\boxed{d^2_{R'} = \frac{\delta^2}{6}R\delta^2\left(\frac{r'}{\delta}\right)\sin^2\theta'\left[\left(\frac{r'}{\delta}\right) + \cos\theta' - \left(\frac{r}{\delta}\right)\cos\left(\theta' - \theta\right)\right] + \mathcal{O}(L^5)} \tag{5.28}$$

where d_{Eu} is the distance between p' and q' if curvature R is set to 0, and $d_{R'}$ is the curvature-dependent modification to this Euclidean distance. The next term in the distance equation is given by

$$\begin{aligned} d^2_R &= -\frac{1}{3}R_{\mu\alpha\nu\beta}x^{\mu}_q x^{\alpha}_{q'} x^{\nu}_q x^{\beta}_{q'} \\ &= -\frac{R_{1212}}{3}\left[\left(x^1_q x^2_{q'}\right)^2 + \left(x^2_q x^1_{q'}\right)^2 - 2\,x^2_q x^1_{q'} x^1_q x^2_{q'}\right] \end{aligned}$$

$$= \frac{R}{6}\Big[2\,(r)^2 \sin\theta\cos\theta \;\; w\,(r',\theta')\,(\delta + w\,(r',\theta')\cos\theta')\sin\theta' \\ - (r\cos\theta\, w\,(r',\theta')\sin\theta')^2 - (r)^2\sin^2\theta\,(\delta + w\,(r',\theta')\cos\theta')^2\Big]$$

$$\boxed{\implies d_R^2 = \frac{\delta^2}{6}R\delta^2\left(\frac{r}{\delta}\right)^2\left[\left(\frac{r'}{\delta}\right)\left(1+\left(\frac{r'}{\delta}\right)\cos\theta'\right)\sin 2\theta\sin\theta' \\ - \left(\frac{r'}{\delta}\right)^2\cos^2\theta\sin^2\theta' - \sin^2\theta\left(1+\left(\frac{r'}{\delta}\right)\cos\theta'\right)^2\right] + \mathcal{O}\left(L^6\right)} \tag{5.29}$$

We may now rewrite the complete distance d as

$$\boxed{d = \sqrt{d_{\text{Eu}}^2 + d_{R'}^2 + d_R^2} = d_{\text{Eu}} + \frac{d_{R'}^2 + d_R^2}{2d_{\text{Eu}}} + \mathcal{O}\left(L^5\right)} \tag{5.30}$$

Note that this expansion can be carried out because $d_{R'}^2, d_R^2 \sim \mathcal{O}\left(R\delta^2\right)$. However, due to the presence of $\sqrt{d_{\text{Eu}}^2}$ in the denominator, this term in the integrand can not be integrated for $\epsilon > 1/2$ as, in this case, $B_p^\epsilon \cap B_{p'}^\epsilon \neq \emptyset$. For $x \in B_p^\epsilon \cap B_{p'}^\epsilon$, as $d_{\text{Eu}}(x,x) = 0$, this would cause the integrand to become singular in this region, leading to failure of this expansion.

In order to evaluate eq. (5.7), we require the volume form dV of Σ, in the polar coordinates (r,θ) in B_p^ϵ, and (r',θ') in $B_{p'}^\epsilon$, as well as the volumes of B_p^ϵ and $B_{p'}^\epsilon$ given by $vol\big(B_p^\epsilon\big)$ and $vol\Big(B_{p'}^\epsilon\Big)$ respectively. The volume form in the Cartesian RNCs is given by

$$dV = \sqrt{h_{11}h_{22} - (h_{12})^2}\, dx^1 \wedge dx^2 \tag{5.31}$$

Upon transforming eq. (5.31) into polar coordinates (r,θ) for point $q \in B_p^\epsilon$, we may evaluate the volume form on B_p^ϵ using 5.12, resulting in

$$\boxed{dV_q = \sqrt{h(r,\theta)}\, dr\wedge d\theta = r\sqrt{1 - \frac{R}{6}(r)^2 + \mathcal{O}\left(L^3\right)}\, dr\wedge d\theta \\ = \left[\delta\left(\frac{r}{\delta}\right)\left(1 - \frac{R\delta^2}{12}\left(\frac{r}{\delta}\right)^2\right) + \mathcal{O}\left(L^4\right)\right] dr\wedge d\theta} \tag{5.32}$$

Similarly, eq. (5.31) can be transformed into polar coordinates (r',θ') for point $q' \in B_{p'}^\epsilon$, resulting in the volume form on $B_{p'}^\epsilon$:

$$
\begin{aligned}
dV_{q'} &= \sqrt{h(r',\theta')}\, dr' \wedge d\theta' \\
&= \frac{w^2(r',\theta')}{r'} \left(1 - \frac{1}{6} R \left[\delta^2 + w^2(r',\theta') + 2\delta w(r',\theta') \cos\theta'\right] + \mathcal{O}(L^3)\right)^{1/2} dr' \wedge d\theta' \\
\implies & \boxed{dV_{q'} = \left[\delta\left(\frac{r'}{\delta}\right)\left(1 - \frac{R\delta^2}{12}\left[\left(\frac{r'}{\delta}\right)^2 + 2\left(\frac{r'}{\delta}\right)\cos\theta' + \cos 2\theta'\right]\right) + \mathcal{O}(L^4)\right] dr' \wedge d\theta'}
\end{aligned}
\tag{5.33}
$$

These volume elements can be integrated over B_p^ϵ and $B_{p'}^\epsilon$ respectively, resulting in

$$
\begin{aligned}
vol\big(B_p^\epsilon\big) &= \int_{\theta=0}^{\theta=2\pi} d\theta \int_{r=0}^{r=\epsilon} dr\, r \left(1 - \frac{r^2}{12} R\right) + \mathcal{O}(L^5) \\
&= \pi\epsilon^2 - \epsilon^4 \frac{\pi}{24} R + \mathcal{O}(L^5)
\end{aligned}
$$

A similar calculation results in $vol\Big(B_{p'}^\epsilon\Big)$ and the product $vol\big(B_p^\epsilon\big) \times vol\Big(B_{p'}^\epsilon\Big)$ as follows:

$$
\begin{aligned}
vol\Big(B_{p'}^\epsilon\Big) &= \int_{\theta'=0}^{\theta'=2\pi} d\theta' \int_{r'=0}^{r'=\epsilon} dr'\, r' \left(1 - \frac{R}{12}\left[r'^2 + 2\delta r' \cos\theta' + \delta^2 \cos 2\theta'\right]\right) + \mathcal{O}(L^5) \\
&= \pi\epsilon^2 - \epsilon^4 \frac{\pi}{24} R + \mathcal{O}(L^5) \\
\implies vol\big(B_p^\epsilon\big) \times vol\Big(B_{p'}^\epsilon\Big) &= \pi^2\epsilon^4 \left[1 - \frac{\epsilon^2}{12} R\right] + \mathcal{O}(L^7)
\end{aligned}
$$

The normalisation constant N is then given by

$$
\boxed{N = \frac{1}{vol\big(B_p^\epsilon\big) \times vol\Big(B_{p'}^\epsilon\Big)} = \frac{1}{\pi^2\epsilon^4}\left[1 + \frac{\epsilon^2}{12} R\right] + \mathcal{O}\left(\frac{1}{L}\right)}
\tag{5.34}
$$

We may now evaluate eq. (5.7), in the form

$$
\bar{d} = N \int_{\theta=0}^{\theta=2\pi} \int_{r=0}^{r=\epsilon} \sqrt{h(r,\theta)}\, dr d\theta \int_{\theta'=0}^{\theta'=2\pi} \int_{r'=0}^{r'=\epsilon} \sqrt{h(r',\theta')}\, dr' d\theta' \left[d_{\text{Eu}} + \frac{d_w^2 + d_R^2}{2 d_{\text{Eu}}} + \mathcal{O}(L^5)\right] \tag{5.35}
$$

evaluating terms up till $\mathcal{O}(\delta^3)$, resulting in an expansion of the ratio $\frac{\bar{d}(p,p')}{\delta}$ and the dimensionless

Ricci curvature $K_P(p,p')$ of the form:

$$\frac{\bar{d}\,(p,p')}{\delta} = c_P + \tilde{c}_R\, R\delta^2 + \mathcal{O}\left(L^3\right) \tag{5.36}$$

$$\boxed{K_P(p,p') = 1 - \frac{1}{c_P}\frac{\bar{d}\,(p,p')}{\delta} = -\frac{\tilde{c}_R}{c_P} R\delta^2 + \mathcal{O}\left(L^3\right)} \tag{5.37}$$

where

$$\tilde{c}_R \equiv \frac{\mu^2}{12} c_P - k_1 - k_2 + k_3 \tag{5.38}$$

$$c_P \equiv \frac{1}{\pi^2\mu^4} \int_{\theta=0}^{\theta=2\pi} \int_{s=0}^{s=\mu} \int_{\theta'=0}^{\theta'=2\pi} \int_{s'=0}^{s'=\mu} ds\, d\theta\, ds'\, d\theta'\ \left[s\, s'\, D_{\text{Eu}}\right] \tag{5.39}$$

$$k_1 \equiv \frac{1}{12\pi^2\mu^4} \int_{\theta=0}^{\theta=2\pi} \int_{s=0}^{s=\mu} \int_{\theta'=0}^{\theta'=2\pi} \int_{s'=0}^{s'=\mu} ds\, d\theta\, ds'\, d\theta'\ \left[s^3\, s'\, D_{\text{Eu}}\right] \tag{5.40}$$

$$k_2 \equiv \frac{1}{12\pi^2\mu^4} \int_{\theta=0}^{\theta=2\pi} \int_{s=0}^{s=\mu} \int_{\theta'=0}^{\theta'=2\pi} \int_{s'=0}^{s'=\mu} ds\, d\theta\, ds'\, d\theta'\ s\, s' \left[(s')^2 + 2s'\cos\theta' + \cos 2\theta'\right] D_{\text{Eu}} \tag{5.41}$$

$$k_3 \equiv \frac{1}{12\pi^2\mu^4} \int_{\theta=0}^{\theta=2\pi} \int_{s=0}^{s=\mu} \int_{\theta'=0}^{\theta'=2\pi} \int_{s'=0}^{s'=\mu} ds\, d\theta\, ds'\, d\theta'\ \left[\frac{s\, s'\, (D_{R'}^2 + D_R^2)}{D_{\text{Eu}}}\right] \tag{5.42}$$

and the functions $D_{\text{Eu}}, D_{R'}$ and D_R are given by

$$\begin{aligned} D_{\text{Eu}} &= \sqrt{(1 + s'\cos\theta' - s\cos\theta)^2 + (s'\sin\theta' - s\sin\theta)^2} \\ D_{R'} &= \sqrt{s'\sin^2\theta'\,[s' + \cos\theta' - s\cos(\theta' - \theta)]} \\ D_R &= s\sqrt{\left[s'\,(1 + s'\cos\theta')\sin 2\theta\sin\theta' - s'^2\cos^2\theta\sin^2\theta' - \sin^2\theta\,(1 + s'\cos\theta')^2\right]} \end{aligned} \tag{5.43}$$

where μ is as defined in eq. (5.11), and the new dimensionless integration variables obtained from the rescaling

$$\begin{aligned} r &= \delta\, s \\ r' &= \delta\, s' \end{aligned} \tag{5.44}$$

are used in integrating the expressions in eqs. (5.27) to (5.29), (5.32) to (5.34) and (5.44). Due to its appearance in the limits of integration, these constants have a non-trivial dependence on μ.

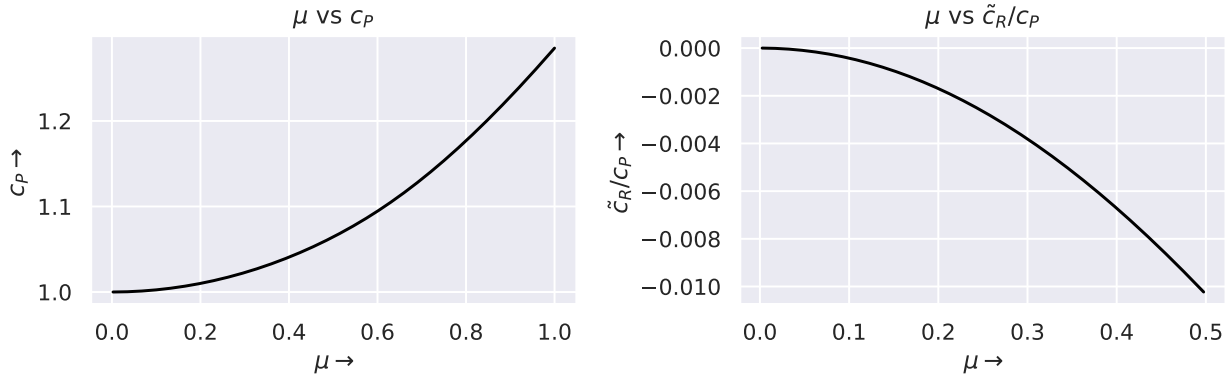

Figure 5.2: Expansion Coefficient behaviour as functions of μ

The plots of c_P and $\tilde{c}_R/c_P$, the leading order coefficients of the ratio $\bar{d}/\delta$ and the dimensionless Ricci curvature K_P (upto a sign) respectively, as functions of μ are given in fig. 5.2.

In the case of spacetimes of higher dimension D, we expect a lot of this analysis to carry through similarly, using hypersperical coordinates. However, in order to fully specify the curvature, we would not only require the Ricci scalar R, but also other invariants constructed from the curvature tensor, such as $R_{ij}v^iv^j$. Having completed our discussion on the manifold calculation of the discrete Ricci curvature, we proceed to describe the construction used to define the causal set discrete Ricci curvature.

5.2 A New Dimensionless Ricci Curvature: The Causet Case

For a D-dimensional spacetime (M, g_{ab}) with Cauchy hypersurface (Σ, h_{ab}), we will consider sprinklings C into M with inextendible antichains $\mathcal{A}$ corresponding to Σ, equipped with the distance function d_ℓ for a mesoscale cutoff ℓ. Our construction is inspired by that of [11], mentioned in section 3.1.3. For $a^*, b^* \in \mathcal{A} \subset C \in \mathcal{C}\,(M, \rho, a^*, b^*)$, we use ϵ radius balls $B^\epsilon_{a^*}$ and $B^\epsilon_{b^*}$ as defined in eq. (5.1), that is,

$$B^\epsilon_{a^*} = \{x \in \mathcal{A} | d_\ell\,(a^*, x) < \epsilon\}\,, \qquad B^\epsilon_{b^*} = \{x \in \mathcal{A} | d_\ell\,(b^*, x) < \epsilon\} \tag{5.45}$$

The average distance between $B^\epsilon_{a^*}$ and $B^\epsilon_{b^*}$ is given by

$$\boxed{\bar{d}\,(a^*, b^*; \epsilon) = \frac{1}{|B^\epsilon_{a^*}|}\frac{1}{|B^\epsilon_{b^*}|}\sum_{x\in B^\epsilon_{a^*}}\sum_{y\in B^\epsilon_{b^*}} d_\ell(x, y)} \tag{5.46}$$

It is to be noted that the average distance is the transport distance associated with the transport plan $\gamma_P : \mathcal{A} \times \mathcal{A} \to [0, \infty)$ given by:

$$\gamma_P(x, y) = m^{\epsilon}_{a^*}(x)\, m^{\epsilon}_{b^*}(y) \tag{5.47}$$

where $m^{\epsilon}_{a^*}$ and $m^{\epsilon}_{b^*}$ are uniform measures defined on $B^{\epsilon}_{a^*}$ and $B^{\epsilon}_{b^*}$ respectively, as in eq. (5.2). This allows for the definition of the **dimensionless Ricci curvature** in the causal set, which we refer to as the "Causet Volume-Induced Ricci Curvature"[2]:

Definition (Causet Volume-Induced Ricci Curvature). The **causet volume-induced Ricci curvature (cVIRC)**, $\kappa_P(a^*, b^*)$, is defined by the equation:

$$\boxed{\kappa_P(a^*, b^*) = 1 - \frac{1}{c_P}\frac{\bar{d}\,(a^*, b^*; \epsilon)}{\delta}} \tag{5.48}$$

where c_P is the continuum value of the ratio $\bar{d}/\delta$, given by eq. (5.39).

This is the quantity whose behaviour we will proceed to explore through numerical simulations in section 6.1. In order to explore its behaviour under the continuum limit $\rho \to \infty$, a procedure similar to that in section 3.1.3 is followed:

The first rooted point a^* is kept fixed across sprinkling densities, but the second rooted point b^* and the ball radius ϵ are made functions of sprinkling density, b^*_ρ, and ϵ_ρ respectively, such that

$$d_\ell\left(a^*, b^*_\rho\right) = \delta_\rho \to 0 \quad \text{as} \quad \rho \to \infty \tag{5.49}$$

$$\epsilon_\rho \to 0 \quad \text{as} \quad \rho \to \infty \tag{5.50}$$

These functions of density need to be specified by us, and we shall take inspiration from the studies of Ollivier curvature on RGGs, as discussed in section 3.1.3. We give the ball radius ϵ_ρ and the inter-center distance δ_ρ, the functional form

$$\epsilon_\rho \sim \rho^{-\alpha} \implies \epsilon_\rho = \epsilon_1 \rho^{-\alpha} \tag{5.51}$$

$$\delta_\rho \sim \rho^{-\beta} \implies \delta_\rho = \delta_1 \rho^{-\beta} \tag{5.52}$$

where α and β are positive constants, and ϵ_1 and δ_1 are the constant values of these quantities at

[2]This dimensionless Ricci curvature is referred to as "volume-induced" due to the use of the volume-induced distance function d_ℓ

unit density. The continuum calculations performed in section 5.1.1 show us that ratio $\bar{d}/\delta$, upon expansion in orders of δ, has at least its highest order, non-trivial coefficient as a function not of δ or ϵ individually, but of the ratio $\mu = \epsilon/\delta$, as given in eqs. (5.39) to (5.42). Therefore, it would be meaningful to maintain this ratio's value across densities, that is,

$$\mu_\rho \equiv \frac{\epsilon_\rho}{\delta_\rho} = \frac{\epsilon_1}{\delta_1}\rho^{\beta-\alpha} = \frac{\epsilon_1}{\delta_1} = \text{const} \implies \alpha = \beta \tag{5.53}$$

In order to set the value of α, we observe that, on the grounds of dimensional analysis, the antichain density $\tilde{\rho}$ can be expected to relate to the sprinkling density ρ as

$$\tilde{\rho} \sim \rho^{\frac{D-1}{D}}$$

Therefore, the number of antichain elements $\left|B_{a^*}^{\epsilon_\rho}\right|$ in a ball of radius ϵ_ρ varies as

$$\left|B_{a^*}^{\epsilon_\rho}\right| \sim \tilde{\rho}\left(\epsilon_\rho\right)^{D-1} \sim \rho^{\frac{D-1}{D}}\,\rho^{-\alpha(D-1)} = \rho^{\frac{D-1}{D}(1-\alpha D)} \sim \tilde{\rho}^{\,1-\alpha D} \tag{5.54}$$

As we increase ρ, while we want the radius ϵ_ρ to decrease as in eq. (5.50), we would like the number of elements in the balls to grow in order to approach the continuum limit, so that the average in eq. (5.46) may approach the continuum average in eq. (5.7). This results in the following functional forms of ϵ_ρ and δ_ρ:

$$\boxed{\begin{aligned} \epsilon_\rho &= \epsilon_1\rho^{-\alpha} \\ \delta_\rho &= \delta_1\rho^{-\alpha} \end{aligned} \qquad \text{where } 0 < \alpha < \frac{1}{D}} \tag{5.55}$$

These constraints on the exponent α prompt the following considerations of the approach to continuum behaviour:

- If α is close to 0, then as $\epsilon_\rho = \epsilon_1\rho^{-\alpha}$ and $\delta_\rho = \delta_1\rho^{-\alpha}$, these quantities will drop off too slowly, resulting in a sub-optimal rate of convergence to the continuum
- If α is close to $1/D$, then as the sizes of balls vary as eq. (5.54), this results in the sizes of balls increasing too slowly, again resulting in a sub-optimal rate of convergence to the continuum

Chapter 6

Implementing Causet Volume-Induced Ricci Curvature for $D = 3$

We now describe the construction used to calculate the **causet volume-induced Ricci curvature** for the simplest case of **flat inextendible antichains in Minkowski spacetime**, and then explore its behaviour as well as that of the predistance function, in the continuum limit, using numerical simulations of sprinklings into Minkowski spacetime. These simulations were performed using code built upon the C++ code framework of [14], and is available here upon request.

6.1 Computational Setup

We now describe the implementation of this construction in code. We begin with describing the process of sprinkling the causal set into **Minkowski spacetime** and the selection of an antichain. We then discuss details regarding the predistance calculation and average distance calculation.

6.1.1 Causet Sprinkling, Antichain Selection and Predistance Calculation

We would like to sprinkle a causal set C into a compact subset of Minkowski spacetime at density ρ and then select an inextendible antichain $\mathcal{A}$ of a given geometry. It is important to mention an important caveat regarding the correspondence between an inextendible antichain $\mathcal{A}$ and the Cauchy hypersurface Σ it is supposed to be approximated by. For a given inextendible antichain $\mathcal{A}$, it is possible to find a Cauchy hypersurface Σ in M that $\mathcal{A}$ embeds into. However, for a given Cauchy hypersurface Σ, no Poisson sprinkling C into the spacetime M will contain an inextendible antichain $\mathcal{A}$ which embeds into Σ, as hypersurfaces are measure-0 sets of a manifold.

Therefore, we can not find a sprinkling C into M with an inextendible antichain $\mathcal{A}$ which embeds into a given Cauchy hypersurface Σ, unless we artificially append a uniform sampling of Σ into an antichain $\mathcal{A}$. While we will artificially append points a^* and b^*_ρ to obtain rooted sprinklings as described in chapter 5, we will not do the same for inextendible antichains. We instead start selecting antichain elements from the base of the spacetime region in consideration and shape the base to have the desired Cauchy hypersurface geometry. We now describe the complete method followed for the case of interest in this work: that of an extrinsically-flat hypersurface Σ at the base of a compact subset U of 3-dimensional Minkowski spacetime M.

- We work with a region U_L of Minkowski spacetime in the shape of a cone, forming the subset of points in the past of the origin at a time coordinate $t \geq -L$ for some integer parameter L, i.e.

$$U_L = \left\{(t, x, y) \in M \middle| -t^2 + x^2 + y^2 \leq 0 \text{ and } -L \leq t \leq 0\right\} \tag{6.1}$$

  The Cauchy hypersurface Σ we are interested is at the base of U_L, given by

$$\Sigma = \left\{(-L, x, y) \in U_L \middle| x^2 + y^2 \leq L^2\right\} \tag{6.2}$$

  We choose U_L to be in the shape of a cone with the Σ its base as U_L is then the future domain of dependence $D^+(\Sigma)$ of Σ. Rooted points a^*, b^*_ρ are also chosen in Σ, and sampled as the first elements of both causal set C and antichain $\mathcal{A}$.

- We begin to sample points about the $t = -L$ slice of U_L. At every integer lattice point $(-L, x, y) \in U_L$, a Poisson random number $n \sim \text{Pois}(\rho)$ is sampled and n points are uniformly sampled into C from the region

$$\left[-L - \frac{1}{2}, -L + \frac{1}{2}\right] \times \left[x - \frac{1}{2}, x + \frac{1}{2}\right] \times \left[y - \frac{1}{2}, y + \frac{1}{2}\right] \cap J^-((0, 0, 0))$$

  Every time a point is sampled, it is compared to every element in the antichain $\mathcal{A}$ defined so far and, if spacelike-separated with every element, is added to $\mathcal{A}$.

- Once the $t = -L$ slice is completed, the process is repeated over the $t = -L+1, \cdots, 0$ slices till the whole region U_L is sampled. This results in a Poisson sprinkling into U_L at density ρ and an iteratively-constructed inextendible antichain $\mathcal{A}$ containing a^*, b^*_ρ. Moreover, since the sampling for $\mathcal{A}$ began from the base of U_L, it ends up taking the shape of this base, with certain thickness Δ in the time-direction. This thickness will go on to contribute to errors and will decrease with increasing ρ.

It is to be noted that this causal set does suffer from boundary effects as we will soon discuss. Therefore, for some $0 < L' < L$, we consider points $(t, x, y) \in C$ to be *padding points* if $t > -\sqrt{x^2 + y^2} - L'$ and *working points* if $t \leq -\sqrt{x^2 + y^2} - L'$. We denote the set of working points by C' and define the set $\mathcal{A}' = \mathcal{A} \cap C'$.[1] For $L = 30$, the constant L' can be set to a value such a 2, which will provide sufficient padding. The code goes further and varies L' with density to maximise utilisation of the points in C.

We will only work $\mathcal{A}'$, which we refer to as the **effective antichain**. In the absence of any curvature, **we use the predistance function instead of the distance function** as discussed in chapter 4. The process described in section 4.2 is followed to find the predistance between a^* and every other element of $\mathcal{A}'$, and the points within predistance ϵ_ρ are taken to define ball $B_{a^*}^{\epsilon_\rho}$. A similar process also defines $B_{b_\rho^*}^{\epsilon_\rho}$, and one such sprinkling with the aforementioned structures is plotted in fig. 6.1. Having defined the necessary balls, the predistances between points across balls and their average is calculated, as in eq. (5.46). Upon changing density ρ, ϵ_ρ and δ_ρ are scaled according to eq. (5.55), for a specified α. It is to be noted that the code is also capable of calculating the complete predistance function over $\mathcal{A}'$, in order to analyse the predistance function error, which allows for understanding the discrete asymptotic silence scale ℓ_{DAS}.

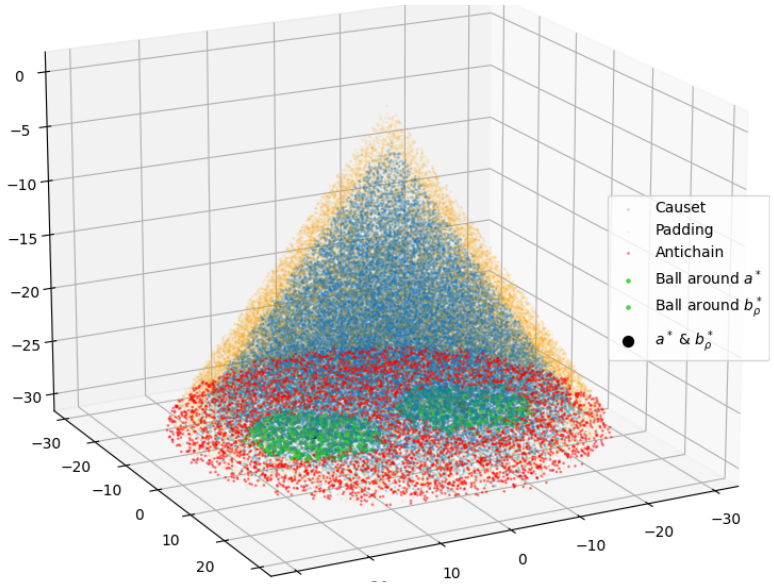

Figure 6.1: Sprinkling with balls at $\rho = 2.5$

[1] Rooted points a^*, b_ρ^* are always chosen to be C'

6.1.2 Additional Features Implemented

These predistance calculations are restricted to points within $\mathcal{A}'$ instead of all of $\mathcal{A}$ as, for a point at the edge of $\mathcal{A}$, while the volume minimising element in the continuum $\mathbf{r}_m$ lies within U_L, the minimising element **e** in the causal set could lie outside C, due to proposition 1. The padding points are therefore added to ensure that even if it does lie outside C', it will lie within C, resulting in accurate predistance calculation. Moreover, a couple of optimisations are implemented in order to speed up calculation:

- During predistance calculation, searches over the common future are restricted to a truncated common future. More specifically, for a given pair of elements $x, y \in \mathcal{A}'$, if the minimising element in the continuum is $\mathbf{r}_m$ at a time coordinate t', then the causal future $J^+(\mathbf{r}_m)$ of $\mathbf{r}_m$ is contained within the common future $J(x, y) \supset J^+(\mathbf{r}_m)$. Since we know the functional form of the volume of $J^+(\mathbf{r}_m)$ up to a time coordinate $t' + \Delta T$, we can find a lower bound on the probability of finding the causal set minimising element **e** in $J(x, y)$ within time coordinate $t' + \Delta T$. We use this relation in order to restrict every causal future search to the region of $J(x, y)$ within time coordinate $t' + \Delta T$ for ΔT such that the probability of **e** being within this search region is a parameter P which is very nearly 1. This parameter was set by hand to $1 - 10^{-11}$. A similar procedure is used to determine the padding size L'.

- The search for the balls $B^{\epsilon_\rho}_{a^*}$ and $B^{\epsilon_\rho}_{b^*_\rho}$ can be restricted to a sufficiently large neighbourhood of a^* and b^*_ρ instead of the entirety of $\mathcal{A}'$. This region is chosen based on the radius ϵ_ρ and the discrete asymptotic silence scale ℓ_{DAS}.

- Finally, as the simulations were performed for an extrinsically flat 2-dimensional hypersurface Σ with translational symmetry, instead of shifting only the second rooted point b^*_ρ with ρ, both rooted points a^*_ρ and b^*_ρ are shifted with ρ, such that the scaling relations in eq. (5.55) are obeyed. This results in a more symmetric setup, as seen in fig. 6.1, where the coordinates of the rooted points are given by

$$a^*_\rho = \left(-\frac{\delta_\rho}{2}, 0, 0\right)$$
$$b^*_\rho = \left(\frac{\delta_\rho}{2}, 0, 0\right)$$

We now describe the tests performed using the described setup. The results of these tests are presented in chapter 7 and discussed in chapter 8.

6.2 Numerical Tests

6.2.1 Test I: Predistance Function Characteristics

Before exploring the average ball distance, we would like to better characterise the predistance function on these antichains. Therefore, we choose a smaller L parameter value of 20 and compute the complete predistance function $\tilde{d}(x,y)\,,\ \forall x,y \in \mathcal{A}'$, for a sprinkling at a particular density ρ. As we are considering a completely flat Cauchy hypersurface, we also calculate the continuum distance $d_h(x,y)\,,\ \forall x,y \in \mathcal{A}'$ where d_h is the distance function defined using the induced metric h_{ab} on Σ. This allows us to calculate the **predistance error function** $\Delta : \mathcal{A}' \times \mathcal{A}' \to \mathbb{R}$, defined as

$$\Delta(x,y) = \frac{\tilde{d}(x,y) - d_h(x,y)}{d_h(x,y)} \tag{6.3}$$

We note here that, in order to calculate the continuum distance d_h, we must assume that $\mathcal{A}' \subset \Sigma$ which, in practice, involves projecting $\mathcal{A}'$ onto Σ with the hopes that the error introduced by this projection dies down at high enough densities. The predistance error function serves as our primary means of characterising the behaviour of the predistance function. As discussed in section 4.3.1, the predistance function will overestimate the continuum distance on average, with this overestimation being more extreme for smaller values of d_h. Therefore, upon plotting a scatter plot of $\Delta(x,y)$ versus $d_h(x,y)\,,\ \forall x,y \in \mathcal{A}'$, we expect a set of points with mostly positive error, decreasing with increasing d_h.

Moreover, an important consideration that can be made in this regard is that of dimension-free predistance. The causal set predistance function can be rewritten as

$$\tilde{d}(a,b) = (\rho)^{-1/D}\left[2\left(\frac{N(\mathbf{e})}{\zeta_D}\right)^{1/D}\right] = \ell_\rho\left[2\left(\frac{N(\mathbf{e})}{\zeta_D}\right)^{1/D}\right] \tag{6.4}$$

where ℓ_ρ is discreteness scale defined in section 4.3.2. Therefore, we see that dimensionality[2] of the predistance arises entirely from the discreteness scale and, upon factoring out the discreteness scale, we get a measure of distance in the units of the discreteness scale. This is a quantity independent of the property of the embedding, i.e., the embedding density ρ, which we refer to as the **dimension-free predistance** $\tilde{D}$, a function purely of the antichain structure:

$$\tilde{D}(x,y) = \frac{\tilde{d}(a,b)}{\ell_\rho} = 2\left(\frac{N(\mathbf{e})}{\zeta_D}\right)^{1/D} \tag{6.5}$$

[2]Here, dimensionality refers to the dimension of length as opposed to the spacetime dimension D

More generally, any length associated with the causal set has a dimension-free quantity associated with it, obtained in a similar manner. In our simulation setup, while the scale of the spacetime region is kept constant across densities, determined by the parameter L, the dimension-free scale, given by $L\ell_\rho^{-1} = \rho^{1/d}L$ does grow with density. Moreover, while the scale of discrete asymptotic silence is expected to shrink with density, disappearing in the continuum limit, the dimension-free scale of discrete asymptotic silence remains fixed across densities. This would suggest that the aforementioned error function

$$\Delta(x,y) = \frac{\tilde{d}(x,y) - d_h(x,y)}{d_h(x,y)} = \frac{\tilde{D}(x,y) - \ell_\rho^{-1} d_h(x,y)}{\ell_\rho^{-1} d_h(x,y)} \tag{6.6}$$

upon being plotted over a **dimension-free continuum distance**

$$\ell_\rho^{-1} d_h \tag{6.7}$$

must have near identical profiles across densities, with the density only determining the extent of the plot. Therefore, this $L = 19$ setup is repeated sprinkled into at densities ranging from $\rho = 0.5$ to $\rho = 3.0$. At each density, the domain of $\ell_\rho^{-1} d_h$ is uniformly binned, and the mean and standard deviation of the error values within each bin are used to obtain a line plot with a 1σ error region about it. The plots at various densities are then overlayed to test this prediction and the results of this test are reported in section 7.1

We now proceed to investigate the behaviour of the average ball distance and hence, the causet volume-induced Ricci curvature. We mention here that due to the boundedness of the region we work with, for a given value of L, there is a trade-off between the values of δ_1 and ϵ_1 that needs to be considered:

1. If one considers well-separated balls, with a large[3] inter-centre distance constant δ_1, we are forced to keep the ball radii small in order to keep them within the region $\mathcal{A}'$, resulting in a small ball radius constant ϵ_1

2. If one considers balls of large radius constant ϵ_1, then one is forced to push these balls close to each other, resulting in a small inter-centre distance constant δ_1, in order to keep both balls within the region $\mathcal{A}'$

[3] In this discussion, a length scale being "large" implies that it is beyond the ℓ_{DAS} length scale, and it being "small" implies it is within the ℓ_{DAS} length scale

Therefore, the ideal scenario, of well-separated balls of large radius, will require very large system sizes, with large L values. As this is computationally very expensive, we do not implement this case, instead choosing to explore the extremes of this trade-off and a middle ground that could be ideal. The configurations at unit density are now specified, with the density scaling of the system given by eq. (5.55) with $\alpha = \frac{1}{2D}$ and L being independent of density. While not evident currently, the discussion of the predistance function characteristics in chapter 8 will justify the consideration of these setups in light of the cases mentioned above.

In each setup, for a set of densities $\{\rho_i\}_{i\in I}$, ensembles of sprinklings are obtained at each density ρ_i, and for each such ensemble, the ensemble average value is found:

$$\left\langle \frac{\bar{d}\left(a^*_{\rho_i}, b^*_{\rho_i}; \epsilon_\rho\right)}{\delta_{\rho_i}} \right\rangle \tag{6.8}$$

These ensemble averages are considered to actually convey the curvature information of the hypersurface they approximate as opposed to the values for the individual sprinklings, in accordance with the statistical interpretation of causal set theory. This set of average values is plotted against the corresponding densities $\{\rho_i\}_{i\in I}$, in order to investigate its convergence in the continuum limit to the continuum value of c_P. This allows for a similar plot of the causet volume-induced Ricci curvature

$$\left\langle \kappa_P\left(a^*_\rho, b^*_\rho\right)\right\rangle = 1 - \frac{1}{c_P}\left\langle \frac{\bar{d}\left(a^*_{\rho_i}, b^*_{\rho_i}; \epsilon_\rho\right)}{\delta_{\rho_i}} \right\rangle \tag{6.9}$$

obtained from eq. (5.48) with the ensemble average used in accordance with the aforementioned statistical interpretation, and its convergence in the continuum limit. The constant c_P is the ratio given by eq. (5.39), calculated in the continuum. An important consequence of eq. (6.9) is that, in this flat case, the causet volume-induced Ricci curvature can be interpreted as the fractional error in the average causal set distance ratio:

$$\left\langle \kappa_P\left(a^*_\rho, b^*_\rho\right)\right\rangle = 1 - \frac{1}{c_P}\left\langle \frac{\bar{d}\left(a^*_{\rho_i}, b^*_{\rho_i}; \epsilon_\rho\right)}{\delta_{\rho_i}} \right\rangle = \frac{1}{c_P}\left(c_P - \left\langle \frac{\bar{d}\left(a^*_{\rho_i}, b^*_{\rho_i}; \epsilon_\rho\right)}{\delta_{\rho_i}} \right\rangle\right)$$

Therefore, the curvature can be directly used as a measure of the accuracy of the causal set distance ratio, to compare and evaluate the accuracy of these setups.

6.2.2 Test II: Causet Volume-Induced Ricci Curvature Setup 1

In this setup, we explore a system closer to the extreme case 1 of this trade-off. This setup consists of a spacetime region with $L = 29$, with a unit density configuration of balls of radius $\epsilon_1 = 6$, whose centres are separated by distance $\delta_1 = 30$, that is, $\mu = 0.2$. Ensembles of sprinklings of this setup are generated, at densities ranging from $\rho = 1$ to $\rho = 10$, with ensemble sizes ranging from 100 per density at the lower densities to 50 per density at the higher densities.

6.2.3 Test III: Causet Volume-Induced Ricci Curvature Setup 2

This setup consists of a system closer to the extreme case 2 of this trade-off. This setup consists of a spacetime region with $L = 29$, with a unit density configuration of balls of radius $\epsilon_1 = 16$, whose centres are separated by distance $\delta_1 = 16$, that is, $\mu = 1$. Ensembles of sprinklings of this setup are generated, at densities ranging from $\rho = 1$ to $\rho = 5$, with ensemble sizes of 50 per density across densities. Due to the larger sizes of the balls involved, the average predistance calculations in this setup are more computationally expensive, resulting in a lower ensemble size per density.

6.2.4 Test IV: Causet Volume-Induced Ricci Curvature Setup 3

Finally, we consider a system that might serve the purpose of an effective middle ground between setups 1 and 2. This setup consists of a spacetime region with $L = 29$, with a unit density configuration of balls of radius $\epsilon_1 = 12$, whose centres are separated by distance $\delta_1 = 26$, that is, $\mu = 0.46$. Ensembles of sprinklings of this setup are generated, at densities ranging from $\rho = 1$ to $\rho = 12.5$, with ensemble sizes ranging from 100 per density at the lower densities to 50 per density at the higher densities.

Part III

Results, Discussion and Conclusion

Chapter 7

Simulation Results

We now present the results of the simulations performed using the setups detailed in chapter 6. The results of this chapter are discussed in chapter 8.

7.1 Test I: Predistance Function Characteristics

As described in section 6.2.1, a Poisson sprinkling is performed with $L = 19$ at density $\rho = 2$, and the complete scatter plot obtained of $\Delta(x, y)$ versus $d_h(x, y)$ is given in fig. 7.1a. The high error points at short continuum distance d_h are then truncated to obtain fig. 7.1b, revealing further detail in the large d_h regime.

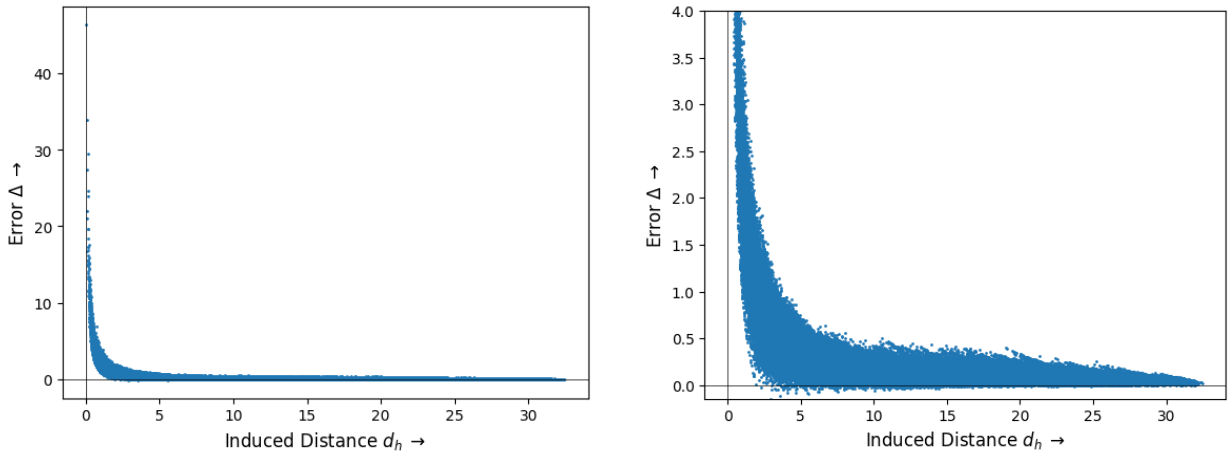

(a) Complete Predistance error scatter plot

(b) Area of interest in complete plot a

Figure 7.1: Predistance error for sprinkling at $\rho = 2$ with $L = 19$

Moreover, for the same setup, Poisson sprinklings are performed at densities from $\rho = 0.5$ to $\rho = 3.0$. The plots of the error function Δ versus the rescaled dimension-free continuum distance $\ell_\rho^{-1} d_h$ at multiple densities are displayed in fig. 7.2. As there are 21 density plots, at densities uniformly spaced between $\rho = 0.5$ and $\rho = 3.0$, in order to compare the profiles of these curves and their error regions, we present 3 separate plots, each containing the overlayed plots of 7 densities: fig. 7.2a containing densities $\rho = 0.5, 0.625, 0.75, 0.875, 1.0, 1.125$ and 1.25, fig. 7.2b containing densities $\rho = 1.375, 1.5, 1.625, 1.75, 1.875, 2.0$ and 2.125, and fig. 7.2c containing densities $\rho = 2.25, 2.375, 2.5, 2.625, 2.75, 2.875$ and 3.0. Finally in order to compare the curves across figs. 7.2a to 7.2c, all 21 of these plots are overlayed together in fig. 7.2d.

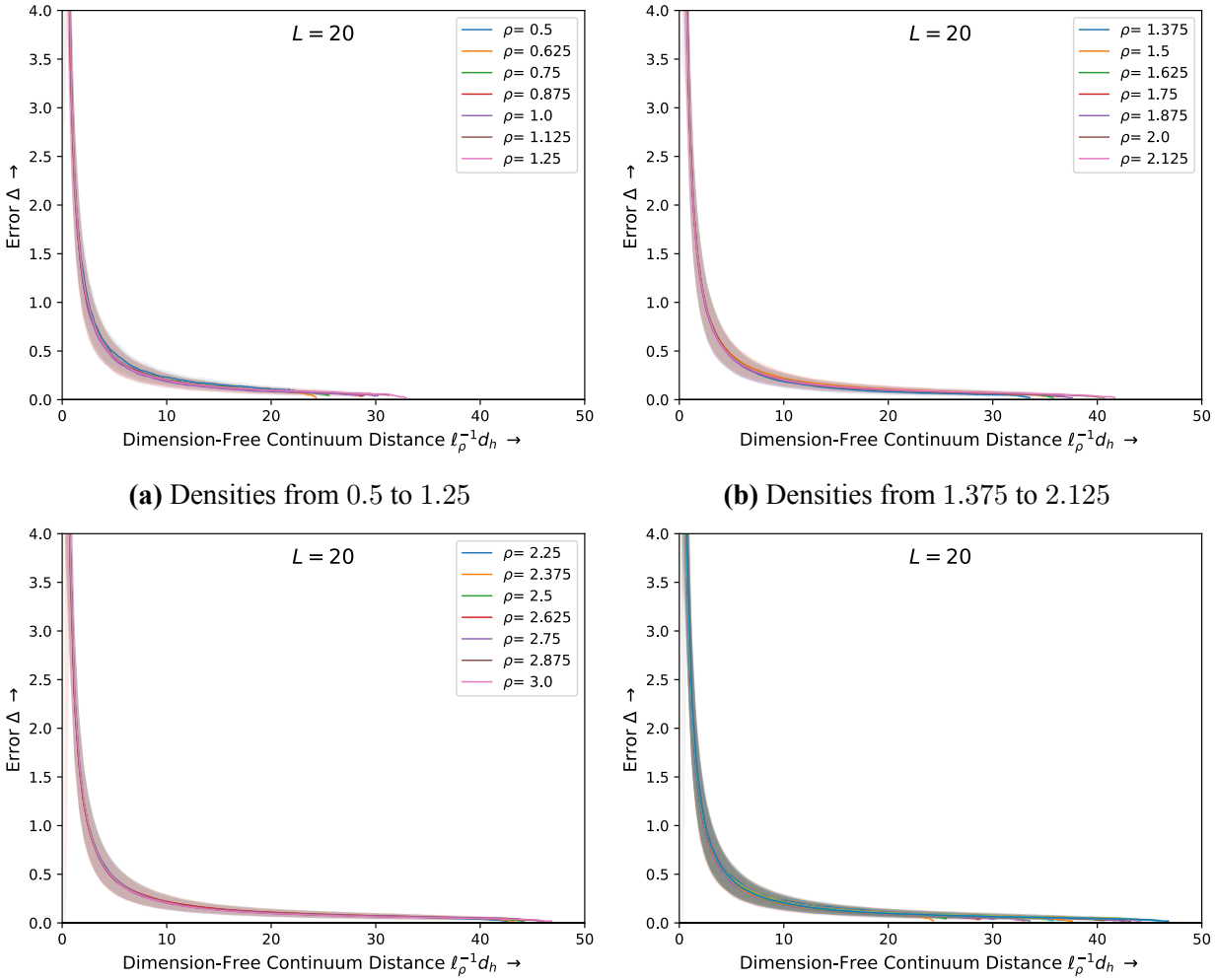

(a) Densities from 0.5 to 1.25

(b) Densities from 1.375 to 2.125

(c) Densities from 2.125 to 3.0

(d) Overlay of all densities from a, b and c

Figure 7.2: Dimension-free error plots across sprinkling densities

7.2 Causet Volume-Induced Ricci Curvature Setups

Sprinklings are performed as described in sections 6.2.2 to 6.2.4 and, at a handful of densities, the following properties of these sprinklings at each of these densities are displayed:

- $|C|$, the ensemble average of causal set size
- $|\mathcal{A}'|$, the ensemble average of effective antichain size
- $\bar{t}$, the ensemble average of the average time coordinate of $\mathcal{A}'$
- Δt, the ensemble average of the standard deviation of the time coordinate of $\mathcal{A}'$
- $\left|B^{\epsilon_\rho}_{a^*_\rho}\right|$, the ensemble average of the size of ball $B^{\epsilon_\rho}_{a^*_\rho}$
- $\left|B^{\epsilon_\rho}_{b^*_\rho}\right|$, the ensemble average of the size of ball $B^{\epsilon_\rho}_{b^*_\rho}$

The quantity $\bar{t}$ is used to indicate the time coordinate of the Cauchy hypersurface Σ that the inextendible antichains approximate, and Δt is used to measure the thickness of effective antichains produced. Also displayed are the plots of κ_P and $\langle \overline{d}/\delta \rangle$ versus ρ, as described in section 6.2, along with their continuum values of 0 and c_P respectively. The error bars in these plots correspond to a standard error of 1σ.

7.2.1 Test II: Causet Volume-Induced Ricci Curvature Setup 1

ρ	$\lvert C\rvert$	$\lvert\mathcal{A}'\rvert$	$\bar{t}$	Δt	ϵ_ρ	$\left\lvert B^{\epsilon_\rho}_{a^*_\rho}\right\rvert$	$\left\lvert B^{\epsilon_\rho}_{b^*_\rho}\right\rvert$
1.00	26900.233	2423.058	-28.647	0.346	6.000	42.6699	42.6311
2.00	53778.420	3950.060	-28.976	0.297	5.345	61.0100	60.8000
3.00	80633.520	5233.800	-28.991	0.279	4.996	73.8300	74.5800
4.00	107456.170	6349.770	-28.997	0.269	4.762	84.9300	85.3700
5.00	134415.100	7371.940	-29.001	0.263	4.588	95.8100	97.9700
6.00	161330.660	8319.160	-29.003	0.259	4.451	103.7600	105.4000
7.00	188124.950	9191.211	-29.004	0.255	4.338	111.4210	112.4740
8.00	215111.950	10034.110	-29.005	0.253	4.242	118.3400	119.8200
9.00	241946.500	10816.350	-29.006	0.250	4.160	124.3000	123.6900
10.00	268863.940	11584.430	-29.007	0.248	4.088	130.9000	129.1400

Table 7.1: Properties of Sprinklings in cVIRC Setup 1

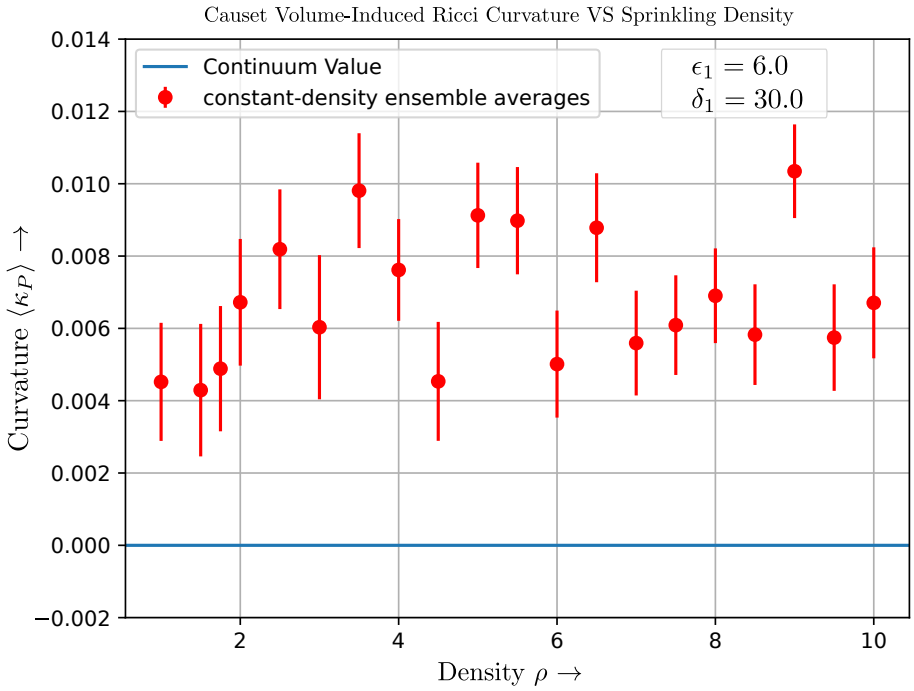

Figure 7.3: cVIRC Setup 1: Curvature Plot

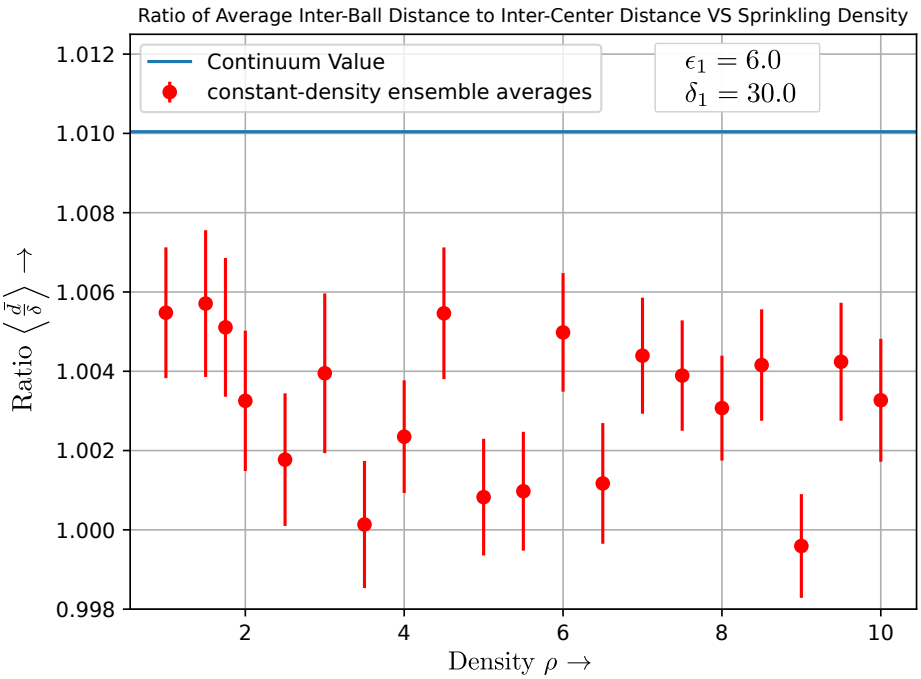

Figure 7.4: cVIRC Setup 1: Distance Ratio Plot

7.2.2 Test III: Causet Volume-Induced Ricci Curvature Setup 2

ρ	$\lvert C\rvert$	$\lvert\mathcal{A}'\rvert$	$\bar{t}$	Δt	ϵ_ρ	$\left\lvert B^{\epsilon_\rho}_{a^*_\rho}\right\rvert$	$\left\lvert B^{\epsilon_\rho}_{b^*_\rho}\right\rvert$
1.0	26906.018	2417.236	-28.930	0.344	16.000	571.509	569.836
1.5	40346.792	3233.472	-28.960	0.314	14.954	672.264	678.491
2.0	53747.620	3943.280	-28.978	0.296	14.254	757.360	754.540
2.5	67213.521	4606.271	-28.986	0.286	13.734	829.479	829.521
3.0	80634.844	5221.000	-28.989	0.280	13.323	884.778	881.800
3.5	94109.189	5799.698	-28.993	0.274	12.985	942.792	939.849
4.0	107637.110	6361.574	-28.998	0.269	12.699	987.556	991.481
4.5	120974.580	6873.680	-28.998	0.266	12.452	1031.740	1035.460
5.0	134394.260	7368.200	-29.001	0.264	12.236	1070.700	1075.460

Table 7.2: Properties of Sprinklings in cVIRC Setup 2

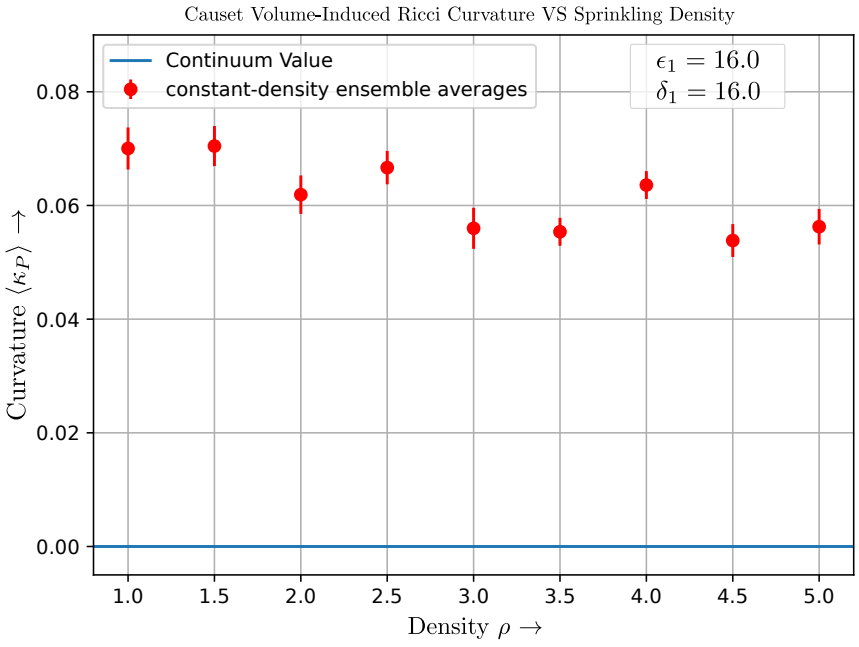

Figure 7.5: cVIRC Setup 2: Curvature Plot

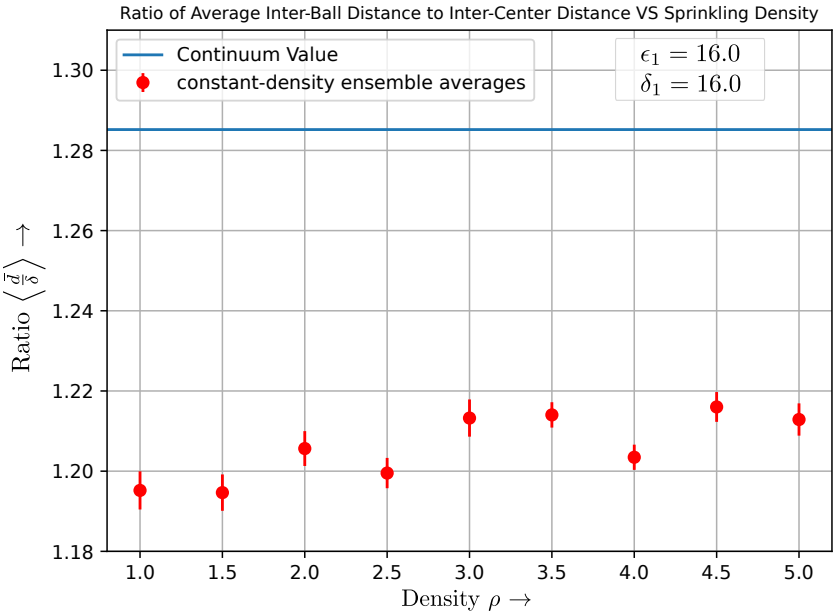

Figure 7.6: cVIRC Setup 2: Distance Ratio Plot

7.2.3 Test IV: Causet Volume-Induced Ricci Curvature Setup 3

ρ	$\lvert C\rvert$	$\lvert\mathcal{A}'\rvert$	$\bar{t}$	Δt	ϵ_ρ	$\left\lvert B^{\epsilon_\rho}_{a^*_\rho}\right\rvert$	$\left\lvert B^{\epsilon_\rho}_{b^*_\rho}\right\rvert$
1.00	26895.536	2425.906	-28.931	0.345	12.000	289.138	290.217
2.00	53790.211	3937.905	-28.978	0.296	10.690	386.137	386.221
3.00	80625.510	5217.390	-28.990	0.279	9.992	457.000	456.160
4.00	107523.480	6351.070	-28.997	0.270	9.524	514.700	514.530
5.00	134419.530	7379.184	-29.001	0.263	9.177	559.439	560.949
6.00	161422.850	8324.940	-29.002	0.259	8.902	594.740	599.490
7.00	188259.640	9210.130	-29.005	0.256	8.676	632.890	634.160
8.00	215100.400	10030.480	-29.005	0.253	8.485	663.090	660.070
9.00	241938.700	10821.990	-29.006	0.250	8.320	691.556	691.078
10.00	268875.000	11578.160	-29.008	0.248	8.176	720.800	719.400
11.00	295645.640	12306.720	-29.006	0.247	8.047	740.780	745.740
12.00	322457.660	12997.040	-29.007	0.245	7.931	767.680	765.500

Table 7.3: Properties of Sprinklings in cVIRC Setup 3

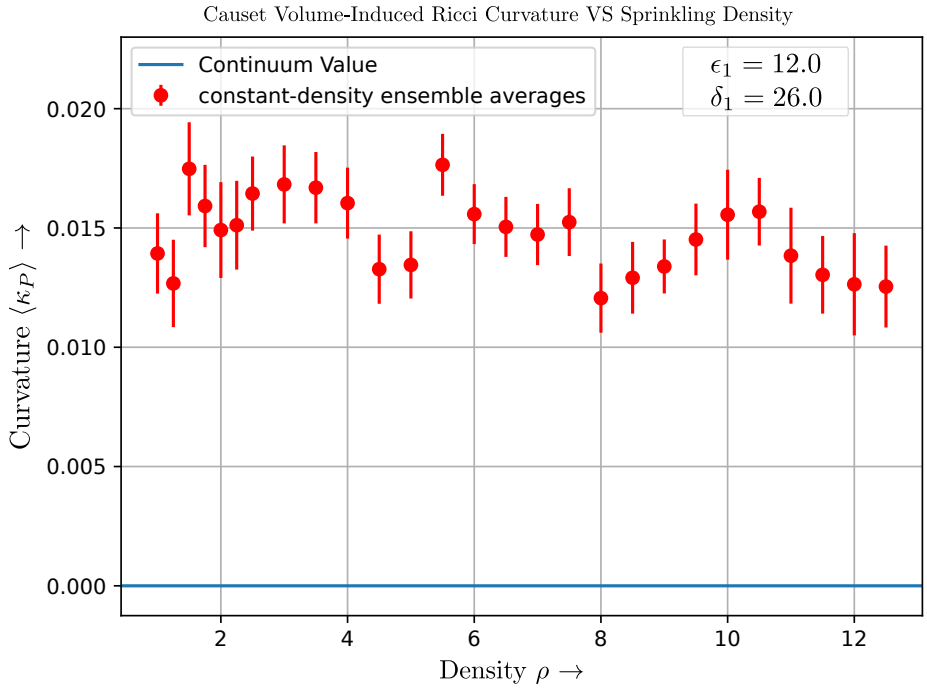

Figure 7.7: cVIRC Setup 3: Curvature Plot

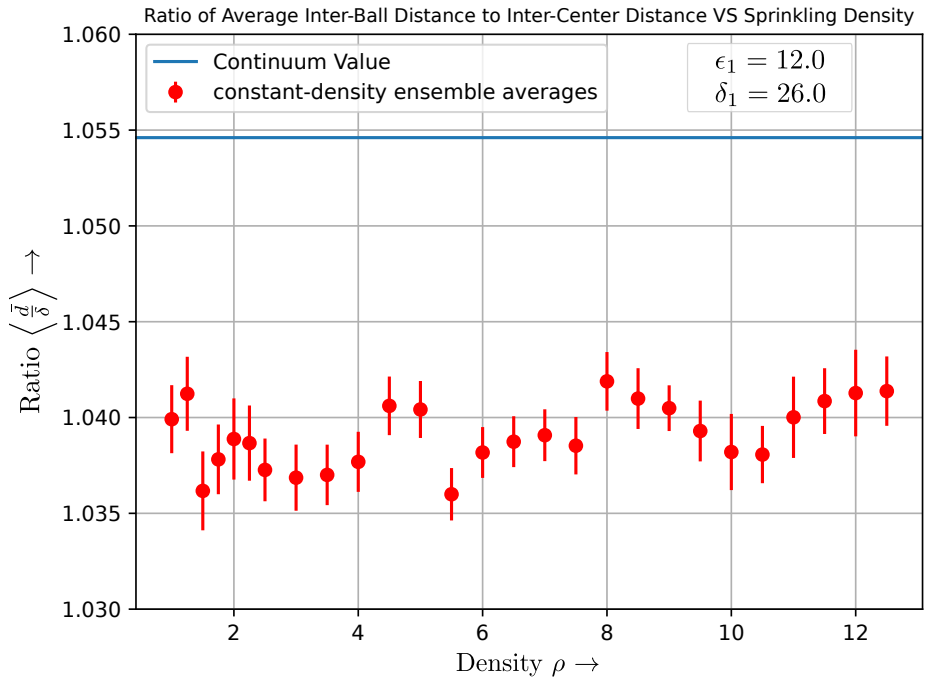

Figure 7.8: cVIRC Setup 3: Distance Ratio Plot

Chapter 8

Discussion

We now discuss the results presented in chapter 7, beginning with the predistance function characterisation in section 6.2.1.

8.1 Predistance Function Characteristics

We see a typical predistance error plot in section 7.1. As explained previously in section 4.3.1, the predistance function greatly overestimates the continuum distance d_h at small values of d_h, resulting in the large error seen in fig. 7.1a. This is the phenomenon of discrete asymptotic silence, which plays the role of the most significant source of error in our analysis of antichain structure. Moreover, we see that this error quickly drops off, seeming to tend to 0 at large d_h. In order to better visualise this decay in error, we use fig. 7.1a and perform the process used to obtain fig. 7.2: we uniformly bin the domain d_h, and find the mean and standard deviation of the error of all points within each bin. We may then use these values to obtain the error plot in fig. 8.1, where the error band represents a 1σ deviation in error. We see that the error effectively drops below 15% past around $d_h = 10$, and reaches its minimum value of around 5% near $d_h = 30$. This plot can then be used to characterise the discrete asymptotic silence scale ℓ_{DAS}, which we may choose to be the continuum distance at which the average error is around 10%, which corresponds roughly between $d_h = 15$ and $d_h = 20$ in this sprinkling. While this characterisation of ℓ_{DAS} applies to graphs at the sprinkling density $\rho = 2$, this error plot will change shape with sprinkling density. This is to be expected, as the discreteness scale $\ell_\rho = (\rho)^{-1/d}$ decreases with sprinkling density, and the effects of this discretisation will also begin to reduce, resulting in further restriction of the regime of discrete asymptotic silence.

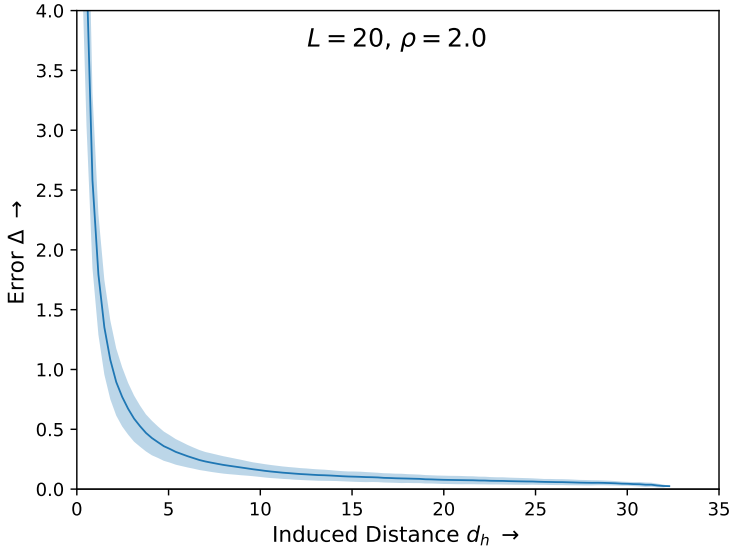

Figure 8.1: Error plot, for $L = 20$ and $\rho = 2$

In order to perform a scale-independent analysis of the predistance error function and discrete asymptotic silence, we use fig. 7.2, wherein the dimension-free continuum distance $\ell_\rho^{-1} d_h$ provides an embedding-independent description of the antichain. We firstly note the high degree of overlap of these plots across densities in fig. 7.2d. This lends credence to the aforementioned prediction of scale independence in these plots, and allows for an absolute characterisation of the discrete asymptotic silence scale, as we see that the error Δ drops below 10% when the continuum distance exceeds around $25\ell_\rho$, which we may use to identify the DAS regime. We note that, across densities, the rescaled error plots in fig. 7.2d tend to deviate from the common trend, and dip towards $\Delta = 0$ at their largest induced distance values. Further investigation is required in order to determine the nature of this deviation for predistances between boundary points in these sprinklings.

8.2 Causet Volume-Induced Ricci Curvature Calculations

We first make some observations about the general behaviour of the sprinklings that were numerically produced, from tables 7.1 to 7.3. We note that, as we increase sprinkling density, the inextendible antichain tends to move closer to the $t = -L$ plane, and seem to settle roughly on this plane at a high enough density. Furthermore, the thickness of these antichains, given by the standard deviation of their time coordinates, decreases with density. Both of these factors result in a more accurate continuum distance d_h and a more accurate correspondence with the Cauchy hypersurface, both in the continuum limit. Finally, as was expected based on the analysis in section 5.2, upon increasing density, although the radii of the balls decrease, the number of elements in the balls increases, which is the desired behaviour of these sprinkling setups.

A general trend observed in the behaviours of cVIRC setups 1, 2 and 3 through figs. 7.3, 7.5 and 7.7 is that the causal set curvatures are consistently greater than the manifold curvature which, from eq. (5.36), is given to be 0. This directly results from the quantity $\langle\frac{\bar{\tilde{d}}}{\tilde{\delta}}\rangle$ for the causal sets underestimating its manifold value as can be seen from figs. 7.4, 7.6 and 7.8. We do not expect the causal set values of these variables to oscillate about their manifold values as discrete asymptotic silence results in stochastic fluctuations with non-zero mean, consistently skewing average causal set variables away from their manifold values. In order to explain the trend in deviation of these quantities from their continuum values, we compare and contrast the corresponding constructions performed in the continuum and the causal set in order to obtain these quantities: For rooted points a^*, b^* belonging to both $\mathcal{A}'$ and Σ, we first use the distance functions d and $d_\ell \equiv \tilde{d}$ to find the ϵ radius balls B^ϵ and $\tilde{B}^\epsilon$ in the Cauchy hypersurface and the inextendible antichain respectively

$$B^\epsilon_{a^*} = \{x \in \Sigma | d\,(a^*, x) < \epsilon\}$$
$$\tilde{B}^\epsilon_{a^*} = \left\{x \in \mathcal{A}' \middle| \tilde{d}\,(a^*, x) < \epsilon\right\}$$

and similarly for $B^\epsilon_{b^*}$ and $\tilde{B}^\epsilon_{b^*}$. Then these balls are used to calculate the average continuum and causal set distances $\bar{d}, \bar{\tilde{d}}$ between the respective balls. The rooted points a^*, b^* are chosen such that $d(a^*, b^*) = \delta$ and the corresponding causal set quantity $\tilde{\delta} = \tilde{d}(a^*, b^*)$ is also calculated. These quantities are used to obtain the ratios $\frac{\bar{d}}{\delta}$ and $\langle\frac{\bar{\tilde{d}}}{\tilde{\delta}}\rangle$ in the continuum and causal set respectively. Finally, these ratios are used identically in eq. (5.48) to obtain the manifold and causet volume-induced Ricci curvatures κ_P and $\tilde{\kappa}_P$ respectively.

For the purpose of this analysis, we assume $\mathcal{A}' \subset \Sigma$, so that $\tilde{B}^\epsilon_{a^*}, \tilde{B}^\epsilon_{a^*} \subset \Sigma$. Then, we see that as, in general, $\tilde{d}(x, y) > d(x, y)\ \forall x, y \in \mathcal{A}'$,

$$x \in \tilde{B}^\epsilon_{a^*} \implies \tilde{d}(a^*, x) < \epsilon \implies d(a^*, x) < \tilde{d}(a^*, x) < \epsilon \implies x \in B^\epsilon_{a^*}$$

Therefore, in general, we see that $\tilde{B}^\epsilon_{a^*} \subset B^\epsilon_{a^*}$ and similarly, $\tilde{B}^\epsilon_{b^*} \subset B^\epsilon_{b^*}$. This is also observed in the results of the numerical simulations, as shown in fig. 8.2 wherein fig. 8.2a is one of the sprinklings from cVIRC setup 1, and fig. 8.2b is one of the sprinklings from cVIRC setup 2, where these plots are obtained by projecting the antichains onto the $t = -L$ plane. Therefore, the points furthest away from the centers are excluded in the causal set cVIRC calculation. As these are the points that contribute the largest distances to the average $\bar{\tilde{d}}$ in the causal set case, their exclusion results in a lowering of the causal set ratio $\langle\frac{\bar{\tilde{d}}}{\tilde{\delta}}\rangle$ with respect to the manifold ratio $\frac{\bar{d}}{\delta}$. This counter-intuitive consequence of DAS then results in the causal set VIRC overestimating the continuum

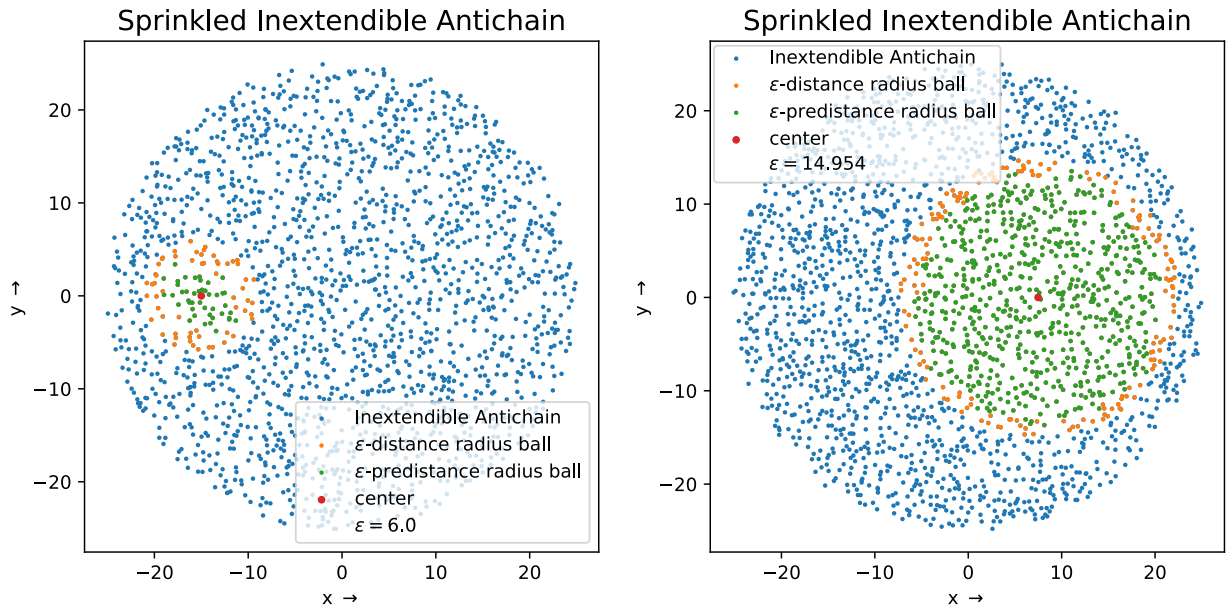

(a) $\tilde{B}^{\epsilon}_{a^*}$ and $B^{\epsilon}_{a^*}$ for $\rho = 1$ and $\epsilon_1 = 6$

(b) $\tilde{B}^{\epsilon}_{b^*}$ and $B^{\epsilon}_{b^*}$ for $\rho = 1.5$ and $\epsilon_1 = 16$

Figure 8.2: Inextendible antichains with predistance and distance-based balls

DRC, as is observed. Moreover, DAS also results in the predistance overestimating all continuum distances, which should result in a larger causal set ratio $\langle \frac{\tilde{d}}{\delta} \rangle$ than the corresponding antichain ratio, with the most extreme consequences to be felt in setup 2 wherein the balls have significant overlap. However, from figs. 7.3, 7.5 and 7.7, we see that this effect does not seem to contribute significantly to the curvature in comparison to the effect of ball underestimation.

Beyond this general trend, we see that some setups better estimate the manifold curvature, with setup 1 resulting in an antichain curvature with the smallest deviations from manifold curvature and setup 2 resulting in an antichain curvature with the largest deviations from manifold curvature. However, setup 1 is also the least well-behaved, with very large fluctuations with changing density, while setup 2 is the most well-behaved, with small fluctuations in the overall trend of a decreasing antichain curvature with increasing density. This trend in fluctuations can result from the sizes of the balls in the setups; As setup 1 has the smallest ball sizes, it is more susceptible to stochastic fluctuations, as evidenced by the large error bars in fig. 7.3, while setup 2, having the largest ball sizes, is the least affected by these fluctuations, resulting in the small error bars in fig. 7.5.

Given these properties of setups 1 and 2, setup 3 might represent a more ideal compromise between the extreme cases of setups 1 and 2. While the fluctuations in setup 3 are still significant with a

seemingly very slow convergence to continuum curvature, the overall deviation from continuum curvature is comparable to that of setup 1. Setup 3 also provides a computationally economical alternative to setup 2, while still not suffering from the effects of stochastic fluctuation as much as the most computationally economical system of setup 1. Furthermore, since we know that, in the continuum, the cDRC takes the form

$$K_P = -\frac{\tilde{c}_R}{c_P} R\delta^2 + \mathcal{O}\left(\delta^3\right)$$

we can conclude from the behaviour of $\tilde{c}_R/c_P$ from fig. 5.2 that the effects of intrinsic curvature diminish with decreasing μ. Therefore, setup 3 might also computationally benefit from μ being in the neighbourhood of $\mu = 0.5$ as the effects of curvature might still be significant enough to numerically extract out the intrinsic curvature R from the causet volume-induced Ricci curvature κ_P. Therefore, we hypothesise that in order to probe converge to the continuum, an ideal value of the ratio μ lies somewhere in a neighbourhood of $\mu = 0.5$. However, as is evident from the error plots in fig. 7.2, in order to work in a regime wherein the effects of discrete asymptotic silence are completely negligible, one requires systems of discreteness scale much smaller than the system size. Therefore, we may benefit significantly from larger scale simulations which may allow us to observe the behaviour of the cVIRC at a finer scale.

Chapter 9

Conclusion

In this work, we reviewed curvature measures in the literature in order to propose a volume-induced curvature for Cauchy hypersurfaces in the continuum, and for inextendible antichains in causal sets, using the volume-induced distance function. We analytically evaluated the induced continuum curvature for $D = 3$, obtaining a relation between the newly defined curvature and the Ricci curvature of the hypersurface. As a preliminary test, we implemented the inextendible antichain curvature numerically for an antichain corresponding to an extrinsically and intrinsically flat hypersurface in 3-dimensional Minkowski spacetime. We used these numerical results to compare the causal set curvature with that in the continuum and explored the ranges of viability for free parameters in the construction. This has resulted in a curvature variable for inextendible antichains, exhibiting some favourable properties within the limited extents of our flat space simulations, but warranting further study.

Moving forward, we intend to explore the behaviour of the antichain curvature in more general antichains which correspond to intrinsically curved Cauchy hypersurfaces in more general spacetimes, beginning with numerical analysis. This would allow us to observe the behaviour of the curvature, beyond the simplest case of $R = 0$, and determine the computational viability of the quantity. We would also like to analytically derive the antichain curvature, in order to better understand its relation with the continuum curvature, and its behaviour under the continuum limit. This would also allow us to narrow down the range of viable parameters, in order to tune the volume-induced antichain curvature to ensure rapid convergence to the continuum.

Appendix A

Derivation of the volume constant ζ_D

The constant ζ_D is defined as the proportionality constant in the volume V_D of a D-dimensional right circular cone of base radius T and height T:

$$V_D = \zeta_D \, T^D \tag{A.1}$$

In order to derive this expression, we start by deriving the $(D-2)$-dimensional volume of a unit $(D-2)$-sphere S_{D-2}, using it to define the $(D-1)$-dimensional volume of a unit $(D-1)$-ball B_{D-1}, and then the D-dimensional volume V_D of the cone of interest. We begin by using a standard method, beginning with the Gaussian integral

$$\int_{\mathbb{R}} e^{-x^2} \, dx = \sqrt{\pi} \tag{A.2}$$

Exponentiating this equation to the power of $D-1$, and rewriting the integral in hyperspherical coordinates, we get

$$\begin{aligned} \pi^{\frac{D-1}{2}} = \int_{\mathbb{R}^{D-1}} e^{-\sum_{i=1}^{D-1} x_i^2} \prod_{i=1}^{D-1} dx_i &= \int_{S_{D-2}} d\Omega_{D-2} \int_{r=0}^{r=\infty} e^{-r^2} \, r^{D-2} dr \\ &= \Omega_{D-2} \int_{r=0}^{r=\infty} e^{-r^2} \, r^{D-2} dr \end{aligned}$$

where $d\Omega_{D-2}$ is the volume element of the S_{D-2}, which can be integrated to obtain the volume Ω_{D-2} of S_{D-2}, as the integrand is radially symmetric.

This can then be used to evaluate Ω_{D-2}:

$$\pi^{\frac{D-1}{2}} = \frac{\Omega_{D-2}}{2} \int_{t=0}^{t=\infty} e^{-t}\, t^{\frac{D-3}{2}} dt = \frac{\Omega_{D-2}}{2}\, \Gamma\left(\frac{D-1}{2}\right)$$

$$\implies \boxed{\Omega_{D-2} = \frac{2\,\pi^{\frac{D-1}{2}}}{\Gamma\left(\frac{D-1}{2}\right)}}$$

where $\Gamma(z)$ is the gamma function. The volume of unit $(D-1)$-ball B_{D-1} can then be obtained by integrating over the $(D-2)$-sphere slices up to unit radius:

$$B_{D-1} = \int_{r=0}^{r=1} \Omega_{D-2} r^{D-2} dr = \frac{2\,\pi^{\frac{D-1}{2}}}{(D-1)\,\Gamma\left(\frac{D-1}{2}\right)} = \frac{\pi^{\frac{D-1}{2}}}{\left(\frac{D-1}{2}\right)\Gamma\left(\frac{D-1}{2}\right)}$$

$$\implies \boxed{B_{D-1} = \frac{\pi^{\frac{D-1}{2}}}{\Gamma\left(\frac{D+1}{2}\right)}}$$

Finally, by considering an inverted cone with its apex at the origin, and integrating over the $(D-1)$-ball slices of radii r at height r up till $r = T$,

$$V_D = \int_{r=0}^{r=T} B_{D-1} r^{D-1} dr = \frac{\pi^{\frac{D-1}{2}}}{D\,\Gamma\left(\frac{D+1}{2}\right)} T^D$$

$$\implies \boxed{\zeta_D = \frac{\pi^{\frac{D-1}{2}}}{D\,\Gamma\left(\frac{D+1}{2}\right)}}$$

References

[1] Robert M. Wald. General Relativity First Edition. (University Of Chicago Press, 1984). ISBN: 0226870332.

[2] Roger Penrose. Techniques in Differential Topology in Relativity CBMS-NSF Regional Conference Series in Applied Mathematics. (Society for Industrial and Applied Mathematics, 1972). ISBN: 9780898710052.

[3] Sumati Surya. The causal set approach to quantum gravity. In: Living Reviews in Relativity *22*.1 (Sept. 2019). DOI: 10.1007/s41114-019-0023-1. URL: https://doi.org/10.1007%2Fs41114-019-0023-1.

[4] Luca Bombelli et al. Space-time as a causal set. In: Phys. Rev. Lett. *59* (5 Aug. 1987), 521–524. DOI: 10.1103/PhysRevLett.59.521. URL: https://link.aps.org/doi/10.1103/PhysRevLett.59.521.

[5] Luca Bombelli. Statistical Lorentzian geometry and the closeness of Lorentzian manifolds. In: Journal of Mathematical Physics *41*.10 (2000), 6944. DOI: 10.1063/1.1288494. URL: https://doi.org/10.1063%2F1.1288494.

[6] Luca Bombelli et al. *Lorentzian Manifolds and Causal Sets as Partially Ordered Measure Spaces*. 2012. DOI: 10.48550/ARXIV.1212.0601. URL: https://arxiv.org/abs/1212.0601.

[7] Dionigi M. T. Benincasa and Fay Dowker. Scalar Curvature of a Causal Set. In: Physical Review Letters *104*.18 (May 2010). DOI: 10.1103/physrevlett.104.181301. URL: https://doi.org/10.1103%2Fphysrevlett.104.181301.

[8] Philippe Clément and Wolfgang Desch. An elementary proof of the triangle inequality for the Wasserstein metric. In: (2008).

[9] Yann Ollivier. Ricci curvature of Markov chains on metric spaces. In: Journal of Functional Analysis *256*.3 (2009), 810–864. ISSN: 0022-1236. DOI: https://doi.org/10.1016/j.jfa.2008.11.001. URL: https://www.sciencedirect.com/science/article/pii/S002212360800493X.

[10] Pim van der Hoorn et al. Ollivier-Ricci curvature convergence in random geometric graphs. In: Physical Review Research *3*.1 (Mar. 2021). DOI: 10.1103/physrevresearch.3.013211. URL: https://doi.org/10.1103%2Fphysrevresearch.3.013211.

[11] Pim van der Hoorn et al. *Ollivier curvature of random geometric graphs converges to Ricci curvature of their Riemannian manifolds*. 2020. arXiv: 2009.04306 [math.PR].

[12] N. Klitgaard and R. Loll. Introducing quantum Ricci curvature. In: Physical Review D *97*.4 (Feb. 2018). DOI: 10.1103/physrevd.97.046008. URL: https://doi.org/10.1103%5C%2Fphysrevd.97.046008.

[13] N. Klitgaard and R. Loll. Implementing quantum Ricci curvature. In: Phys. Rev. D *97* (10 May 2018), 106017. DOI: 10.1103/PhysRevD.97.106017. URL: https://link.aps.org/doi/10.1103/PhysRevD.97.106017.

[14] Astrid Eichhorn et al. Induced spatial geometry from causal structure. In: Classical and Quantum Gravity *36*.10 (Apr. 2019), 105005. DOI: 10.1088/1361-6382/ab114b. URL: https://doi.org/10.1088%2F1361-6382%2Fab114b.

[15] Michel Buck et al. Boundary terms for causal sets. In: Classical and Quantum Gravity *32*.20 (Sept. 2015), 205004. DOI: 10.1088/0264-9381/32/20/205004. URL: https://doi.org/10.1088%2F0264-9381%2F32%2F20%2F205004.

[16] Astrid Eichhorn et al. Echoes of asymptotic silence in causal set quantum gravity. In: Classical and Quantum Gravity *34*.16 (July 2017), 16LT01. DOI: 10.1088/1361-6382/aa7d1b. URL: https://doi.org/10.1088%2F1361-6382%2Faa7d1b.

[17] Michael B. Cohen et al. *Solving Linear Programs in the Current Matrix Multiplication Time*. 2020. arXiv: 1810.07896 [cs.DS].

[18] Nilas Falster Klitgaard. "New Curvatures for Quantum Gravity". PhD thesis. Nijmegen U., 2022.

[19] Leo Brewin. *Riemann normal coordinates*. http://users.monash.edu.au/leo/research/papers/files/lcb96-01.pdf. Nov. 1996.